Jeppe N. K. Detlefsen (KU-id:mfq130)

3D-printed fiber-coupled vapor-cell magnetometer

Masters Thesis

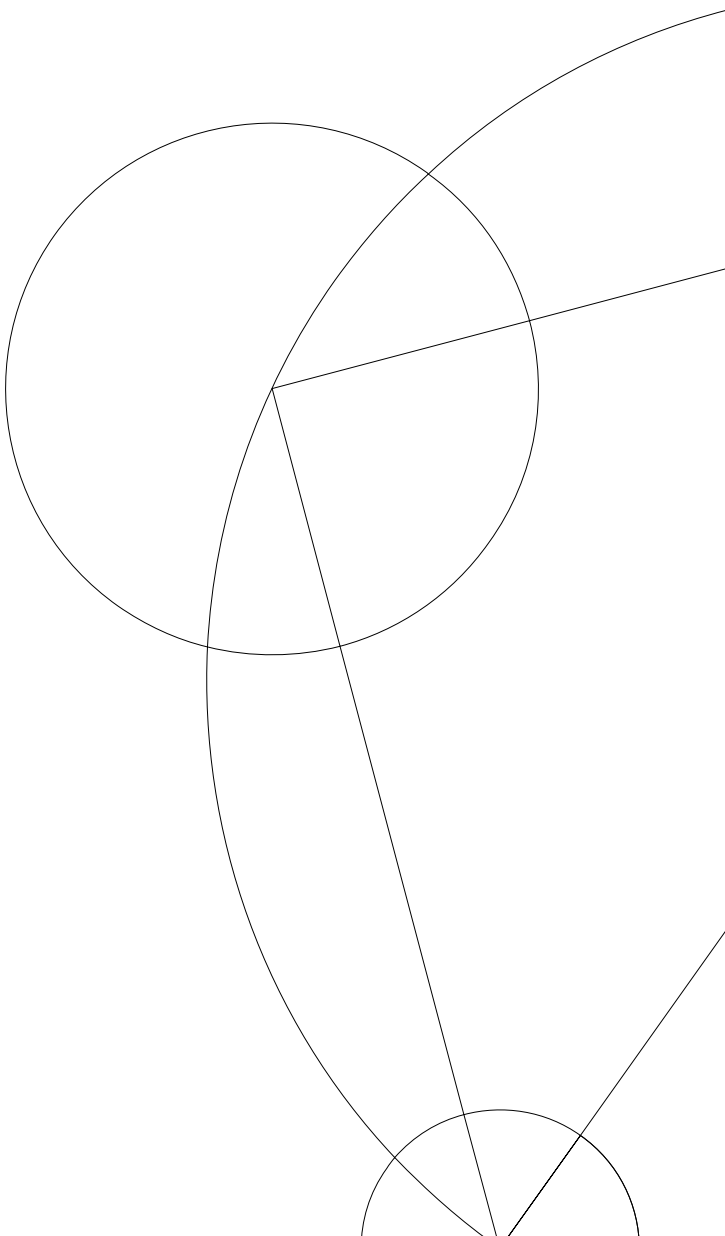

Main supervisor: Prof. Eugene S. Polzik

June 30, 2021

1 Abstract

Magnetometry has many applications in wide range of fields ranging from medical imaging[9] and diagnostics[10][8] to communication and defence[7]. Currently the most sensitive magnetometers are SQUID's (Superconducting quantum interference devices) boasting sensitivities in the $4[fT/\sqrt{Hz}]$ range[3], though they do have several downsides such as cost and their need for cryogenic cooling to maintain their superconducting properties.
To overcome these limitations, we have investigated a magnetometer based on room-temperature caesium vapor. We have successfully constructed and characterized a 3D-printed fiber-coupled magnetometer based on this room-temperature caesium vapour cell.
We have found a sensitivity of $120[fT/\sqrt{Hz}]$ in the range of $5 - 100[Hz]$ and a sensitivity of $74[fT/\sqrt{Hz}]$ at $150[kHz]$. This put us a factor 30 off of the limitation of quantum spin projection noise of $4[fT]$ in the $5 - 100[Hz]$ range.

2 Acknowledgement

Over the course of my masters project at QUANTOP there have been several people that have provided me with a lot of help and insight. First and foremost I would not have had the opportunity to do this work without Professor Eugene Simon Polzik offering me to write my masters thesis under his supervision. I'm very grateful for this opportunity.
In addition I would also like to thank:

- Michael Zugenmaier for providing daily supervision and guidance in the lab.
- Hans Chr. Stærkind for sharing his insight on the best method for assembling the magnetometer.
- Rodrigo A. Thomas for answering my many question.
- Rebecca Schmieg, Karsten Bjerrum Dideriksen and Wenqiang Zheng for being great lab colleagues.

I would also like to extend my gratitude to all the members of the QUANTOP group for being helpful and providing a great work environment.

Contents

List of Figures

3 Introduction

There are many different interesting application for magnetometry, ranging from the searching after oil and mineral deposits, biomedical applications, to finding submerged submarines. One specific example from the bio-medical field is the potential to use a magnetometer to measure a magnetocardiography (MCG) as an alternative to a electrocardiogram (ECG). This may be useful as the MCG does not require physical contact with the patient, which can enable non-invasive measurements of the hearts of fetuses[10]. It may also enable the non-invasive measurement of nerve signals[8]
One of the sensor types with a very good sensitivity is the SQUID (Superconducting quantum interference device) which can have a sensitivity in the $4[fT/\sqrt{Hz}]$ range[3]. But the cost of SQUID's and their need for cryogenic cooling motivates the search for alternative sensor designs.
In this thesis we will explore such an alternative by construction and characterisation of a miniaturized 3D-printed fiber-coupled room temperature vapor cell magnetometer.

We will characterise the magnetometer's performance in 3 different modes of operation: A free induction decay mode (FID) which is a pulsed DC mode, the RF sensitivity, and the continuous DC mode. The magnetometer is designed in the hopes of improving the results in the continuous DC mode compared to what has previously been achieved in our group [10][1]. We hope to achieve this through the suppression of mechanical vibration by having all the optical components mounted in the same rigid 3D printed shell. Even though we expect the sensor to show the largest improvement in the DC regime, we still expect it to have the best sensitivity in the radio frequency domain [17].

4 Theory

4.1 Caesium

In the experiments we will be dealing with a vapor cell containing Caesium-133 isotopes, as it is the only stable isotope of caesium. The distribution of electrons in the different atomic orbitals, also called the electron configuration, can be written as:

$$1s^2 2s^2 2p^6 3s^2 3p^6 4s^2 3d^{10} 4p^6 5s^2 4d^{10} 5p^6 6s^1 \tag{4.1}$$

The notation is composed of a series of element of the form nl^i where n is the principal quantum number which goes from 1 and up in increments of 1 and will indicate the energy level of that orbital. The l indicates the orbital angular momentum of the electrons in the shell, this quantity is also called the "Azimuthal quantum number". The amount of angular momentum is indicated by a letter in order of $\{s, p, d, f, ...\}$ which corresponds to a total angular momentum of $\{0, 1, 2, 3, ...\}$. The i indicates the number of atoms in the shell.
Another way of writing this is $[Xe]6s^1$, which should be read as the electron configuration is the same as in the noble gas Xenon, but with one more electron, called the valence electron. All the dynamics we will be discussing is a result of the different ways we can manipulate the valence electron.

4.1.1 Fine structure & spin-orbit interaction

The spin orbit coupling arises from the magnetic moments of the spin of the electron interacting with the magnetic field that arises from the electron orbiting the nucleus. In general the energy change of such an interaction can be written as

$$\hat{\mathbf{H}}_{\mathbf{SO}} = -\hat{\boldsymbol{\mu}} \cdot \hat{\mathbf{B}} \tag{4.2}$$

In the case of the orbiting electron $\hat{\boldsymbol{\mu}} \propto \hat{\boldsymbol{S}}$ and $\hat{\boldsymbol{B}} \propto \hat{\boldsymbol{L}}$ where $\hat{\boldsymbol{S}}$ is the spin angular momentum and $\hat{\boldsymbol{L}}$ is the orbital angular momentum.

With all the factors we can write the spin-orbit correction as

$$\Delta\hat{\mathbf{H}}_{\mathbf{SO}} = \frac{e^2}{2m_e^2}\frac{1}{r^3}\hat{\boldsymbol{S}} \cdot \hat{\boldsymbol{L}} \tag{4.3}$$

to simplify the solution of the problem we define a quantity which we call the total angular momentum

$$\hat{\boldsymbol{J}} = \hat{\boldsymbol{S}} + \hat{\boldsymbol{L}} \tag{4.4}$$

Since $\hat{\boldsymbol{S}}$ and $\hat{\boldsymbol{L}}$ commute we can rewrite $\hat{\boldsymbol{S}} \cdot \hat{\boldsymbol{L}}$ as

$$\hat{\boldsymbol{S}} \cdot \hat{\boldsymbol{L}} = \frac{1}{2}\left(\hat{\boldsymbol{J}}^2 - \hat{\boldsymbol{S}}^2 - \hat{\boldsymbol{L}}^2\right). \tag{4.5}$$

To calculate the energy correction from this interaction we will take the expectation value of Hamiltonian in equation 4.3, with the state expressed in the basis of $|n, l, j, m_j\rangle$

$$E^{(1)}_{n,l,j,m_J}{}^{SO} = \frac{e^2}{2m_c^2}\langle n, l, j, m_j| \frac{\frac{1}{2}\left(\hat{\boldsymbol{J}}^2 - \hat{\boldsymbol{S}}^2 - \hat{\boldsymbol{L}}^2\right)}{r^3} |n, l, j, m_j\rangle \tag{4.6}$$

We are allowed to use this form of first order non-degenerate perturbation theory because $\frac{\hat{\boldsymbol{S}}\cdot\hat{\boldsymbol{L}}}{r^3}$ commutes with $\hat{\boldsymbol{L}}^2$, the eigenoperator for l, $\hat{\boldsymbol{J}}^2$, the eigenoperator for j, and $\hat{\boldsymbol{J}}_z$, the eigenoperator for m_j. Knowing that the expectation values of our operators are $\left\langle \hat{\boldsymbol{J}}^2 \right\rangle = j(j+1)$, $\left\langle \hat{\boldsymbol{L}}^2 \right\rangle = l(l+1)$, and $\left\langle \hat{\boldsymbol{S}}^2 \right\rangle = s(s+1)$. For more details we will refer you to [4] and now state the result as

$$E^{(1)}_{n,l,j,m_J}{}^{SO} = \frac{\left(E^{(0)}_n\right)^2}{m_e} \frac{n\left[j(j+1) - l(l+1) - \frac{3}{4}\right]}{l(l+\frac{1}{2})(l+1)} \tag{4.7}$$

So in the end we lift the degeneracy between levels which have parallel or anti-parallel orbital angular momentum and spin angular momentum. For this to have an effect we need both the orbital angular momentum and spin angular momentum to be non-zero. The first state that meets this condition is electrons in the first p-orbital. For the p-orbital we have $\{l = 1, s = \frac{1}{2}\}$ which gives $j = \{\frac{1}{2}, \frac{3}{2}\}$. These two levels can be written with the *term symbols* ${}^2P_{\frac{1}{2}}$ and ${}^2P_{\frac{3}{2}}$ respectively.

4.1.2 Hyperfine structure

In the same ways as the fine structure, the hyperfine structure is also the result of a coupling between two magnetic moment. For the hyperfine structure the coupling is between the the electrons total angular momentum $\hat{\boldsymbol{J}}$ and the nuclear magnetic moment $\hat{\boldsymbol{I}}$

$$\hat{\mathbf{H}}_{HFS} = -\hat{\boldsymbol{\mu}} \cdot \hat{\mathbf{B}} \propto \hat{\boldsymbol{I}} \cdot \hat{\mathbf{J}} \tag{4.8}$$

The ${}^2S_{\frac{1}{2}}$ and ${}^2P_{\frac{1}{2}}$ states will split into 2 hyperfine levels as they have $J = \frac{1}{2}$

$$F = |I - J|, ..., |I + J| = |\frac{7}{2} - \frac{1}{2}|, |\frac{7}{2} + \frac{1}{2}| = \{4, 3\} \tag{4.9}$$

and the ${}^2P_{\frac{3}{2}}$ state will split into 4

$$F = |I - J|, ..., |I + J| = |\frac{7}{2} - \frac{3}{2}|, .., |\frac{7}{2} + \frac{3}{2}| = \{2, 3, 4, 5\} \tag{4.10}$$

4.2 Quantized light

To start of our discussion of the quantum mechanical nature of light and later its interaction with an atomic ensemble, we will start with the general expression for the quantized electric field [1]

$$\hat{\mathbf{E}} = \sum_\lambda \sqrt{\frac{\hbar\omega_\lambda}{2\varepsilon_0 V}} \left(\hat{a}_\lambda \mathbf{e}_\lambda e^{i\mathbf{k}_\lambda\cdot\mathbf{r}} + \hat{a}^\dagger_\lambda \mathbf{e}_\lambda e^{-i\mathbf{k}_\lambda\cdot\mathbf{r}}\right) \tag{4.11}$$

where the sum over λ is the sum over all modes, that is all different propagation directions and all different polarizations. $\mathbf{e}_\lambda$ is a unit vector describing the light polarization and as such it is a complex vector. $\mathbf{k}_\lambda$ is the vector that indicates the

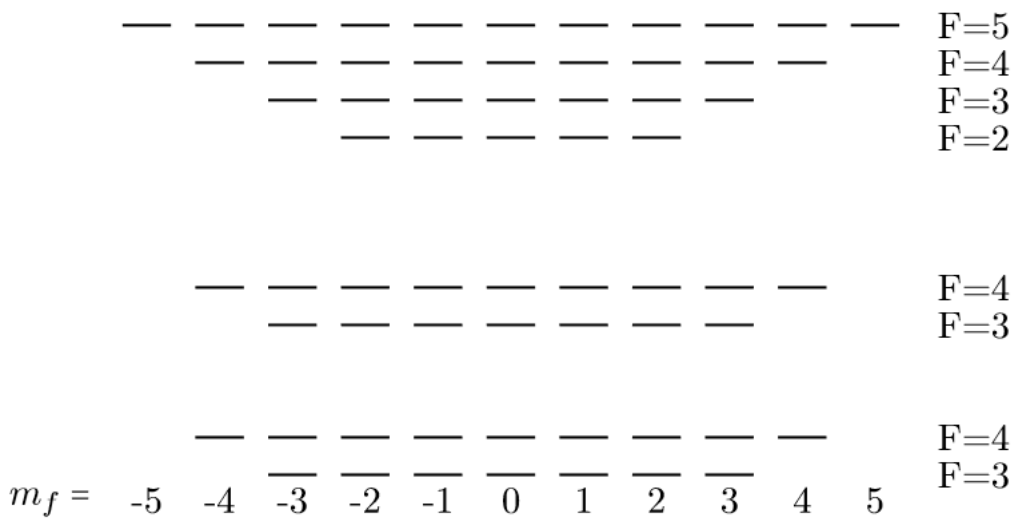

Figure 4.1: Energy level diagram for ceasium-133. This figure shows the relevant levels $S_{1/2}$, $P_{1/2}$ and $P_{3/2}$ (from bottom to top)

propagation direction. ω_λ is the angular frequency of the light. $\hat{a}^\dagger$ and $\hat{a}$ are the creation and annihilation operators respectively. V is the quantsization volume. The annihilation and creation operators have the commutator relation

$$\left[\hat{a}_\lambda, \hat{a}^\dagger_{\lambda'}\right] = \delta_{\lambda,\lambda'} \tag{4.12}$$

and we can define a number operator as

$$\hat{n}_\lambda = \hat{a}^\dagger_\lambda \hat{a}_\lambda \tag{4.13}$$

4.2.1 Stokes operators

Given that we will be working exclusively with polarised light, it makes sense to define a set of quantities that describe how our light is polarized. Normally we have three different basis sets of polarization, that being $\{x, y\}$, $\{+\frac{\pi}{4}, -\frac{\pi}{4}\}$, $\{\sigma_+, \sigma_-\}$, where we usually define the circular polarizations as

$$\sigma_+ = -\frac{x - iy}{\sqrt{2}} \quad \text{and} \quad \sigma_- = \frac{x + iy}{\sqrt{2}}, \tag{4.14}$$

and we can define $\{+\frac{\pi}{4}, -\frac{\pi}{4}\}$ as

$$+\frac{\pi}{4} = \frac{x + y}{\sqrt{2}} \quad \text{and} \quad -\frac{\pi}{4} = \frac{x - y}{\sqrt{2}}. \tag{4.15}$$

Our first guess at defining such a quantity could be to simply take the mean between the amount of one axis minus the amount on the other, as such:

$$S_x = \frac{n_x - n_y}{2} \tag{4.16}$$

if we were to write this on an operator form it would be

$$\hat{S}_x = \frac{\hat{n}_x - \hat{n}_y}{2} = \frac{\hat{a}_x^\dagger \hat{a}_x - \hat{a}_y^\dagger \hat{a}_y}{2} \tag{4.17}$$

and what we have now just constructed is one of the three *Stokes operators*. We can define the other two in a similar fashion and that gives

$$\hat{S}_y = \frac{\hat{n}_{+\frac{\pi}{4}} - \hat{n}_{-\frac{\pi}{4}}}{2} = \frac{\hat{a}_x^\dagger \hat{a}_y + \hat{a}_y^\dagger \hat{a}_x}{2} \tag{4.18}$$

$$\hat{S}_z = \frac{\hat{n}_{\sigma_+} - \hat{n}_{\sigma_-}}{2} = \frac{\hat{a}_x^\dagger \hat{a}_y - \hat{a}_x^\dagger \hat{a}_y}{2i} \tag{4.19}$$

Instead of working in the $\{x, y\}$ basis we may do as in equation 4.14 and define a circular basis as

$$\hat{a}_+ = -\frac{\hat{a}_x - i\hat{a}_y}{\sqrt{2}} \quad \text{and} \quad \hat{a}_- = \frac{\hat{a}_x + i\hat{a}_y}{\sqrt{2}}. \tag{4.20}$$

We can now write two new operators in the circular basis

$$\hat{S}_+ = -\hat{S}_x - i\hat{S}_y \quad \text{and} \quad \hat{S}_- = \hat{S}_x + i\hat{S}_y. \tag{4.21}$$

By using the commutator relation in equation 4.12 we can calculate the commutator relations for the stokes operators

$$\left[\hat{S}_j, \hat{S}_k\right] = i\epsilon_{jkl}\hat{S}_l \quad \text{and} \quad \left[\hat{S}_z, \hat{S}_\pm\right] = \pm\hat{S}_\pm \tag{4.22}$$

These are the same commutator relations that we normally have for angular momentum operators.

As the indices on the stokes operator may indicate or the similarity in the mathematics to the standard treatment of a pure two level system, commonly used in quantum information theory, one may get the inclination that we could construct a sort of Bloch sphere of polarisation state. This is indeed something one can do but when working with polarised light it is no longer called a Bloch sphere but a Poincaré sphere, though the concept is quite similar.

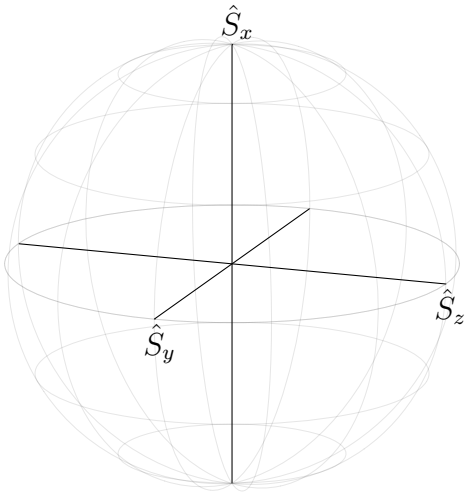

In the case of a high intensity light beam with polarization in the x-direction, the quantum nature of the $\hat{a}_x^\dagger$ and $\hat{a}_x$ may be disregarded and both can just be regarded as a real number. In this case equation 4.17 to 4.19 can be written as

$$S_x \approx \frac{N_x^2 - \hat{a}_y^\dagger \hat{a}_y}{2} \approx \frac{N_x^2}{2} \tag{4.23}$$

$$\hat{S}_y \approx N_x \frac{\hat{a}_y + \hat{a}_y^\dagger}{2} \tag{4.24}$$

$$\hat{S}_z \approx N_x \frac{\hat{a}_y - \hat{a}_y}{2i} \tag{4.25}$$

If we now consider that the light polarization may be different at different positions in time and/or space we will have to introduce spatial and temporal dependency in our stokes operators. Doing this will modify our first commutator relation from 4.22 to

$$\left[\hat{S}_j(z,t), \hat{S}_k(z',t')\right] = i\delta(z-z')\epsilon_{jkl}\hat{S}_l(z,t) \tag{4.26}$$

4.3 Larmor precession

To calculate how the total angular momentum of an atom behaves in an applied external magnetic field we start with a Hamiltonian very similar to the ones in equation 4.2 and 4.8

$$\hat{\mathbf{H}}_{\mathbf{Larmor}} = -\hat{\boldsymbol{\mu}} \cdot \hat{\mathbf{B}}_{\mathbf{ext}}. \tag{4.27}$$

In this case the magnetic moment of the atoms will be $\hat{\boldsymbol{\mu}} = \gamma\hbar\hat{\boldsymbol{F}}$ where γ is the gyromagnetic ratio and $\hat{\boldsymbol{F}} = \left[\hat{F}_x, \hat{F}_y, \hat{F}_z\right]$. If we work in the Heisenberg picture we can use the Heisenberg equation to calculate the time evolution of an operator[13]

$$\frac{d}{dt}\hat{\boldsymbol{A}}(t) = i/\hbar \left[\hat{\boldsymbol{H}}, \hat{\boldsymbol{A}}(t)\right]. \tag{4.28}$$

If we remember that the angular momentum operator in general has the same commutator relation as the first equation in 4.22, we can calculate the equation of motion for the total angular momentum of an atom in an external magnetic field:

$$\frac{d}{dt}\hat{\boldsymbol{F}} = -i/\hbar \left[\hat{\boldsymbol{F}}(\hat{\mathbf{H}}_{\mathbf{Larmor}}) - (\hat{\mathbf{H}}_{\mathbf{Larmor}})\hat{\boldsymbol{F}}\right] \tag{4.29}$$

$$= -i\gamma \left[\hat{\boldsymbol{F}}(\hat{\mathbf{F}} \cdot \hat{\mathbf{B}}_{ext}) - (\hat{\mathbf{F}} \cdot \hat{\mathbf{B}}_{ext})\hat{\boldsymbol{F}}\right] \tag{4.30}$$

$$= \gamma\hat{\boldsymbol{F}} \times \hat{\mathbf{B}}_{ext}. \tag{4.31}$$

From this we see that when subjected to an external magnetic field, the total spin of the atom will precess around an axis defined by the direction of the said magnetic field. This precession will happen with a frequency of $\omega_{Larmor} = \gamma|\mathbf{B}|$. This frequency is called the Larmor frequency.

4.4 Zeeman splitting

When we apply an external magnetic field to our atomic ensemble it will give rise to an interaction as described by equation 4.27. In the same way as the fine structure and hyperfine structure did this will result in an energy level splitting. We can write the Hamiltonian as[14]

$$\hat{H}_{zeeman} = -\hat{\mu}_{atom} \cdot \hat{\mathbf{B}} = g_F\mu_B B F_x, \tag{4.32}$$

where we define $\mathbf{B}$ as the external magnetic field, μ_B is the Bohr magneton and g_F is

$$g_F = \frac{F(F+1) + J(J+1) - I(I+1)}{2F(F+1)}. \tag{4.33}$$

We may also identify the gyromagnetic ratio from earlier as:

$$\gamma = -\frac{g_F\mu_B}{\hbar} \tag{4.34}$$

By using first order time independent perturbation theory and expressing the atomic state with the state vector $|J, I, F, m_F\rangle$, we get the first order energy splitting

$$E^{(1)}_{zeeman} = \hbar\omega_{Larmor} m_f. \tag{4.35}$$

If we were to apply a strong external magnetic field we would also need the second order correction to the energy which has the form [14]

$$E^{(2)}_{zeeman} \propto \frac{16 - m_F^2}{2} B^2. \tag{4.36}$$

A conceptual image of the energy level splitting resulting from the first order from the zeeman effect can be seen in figure 4.2

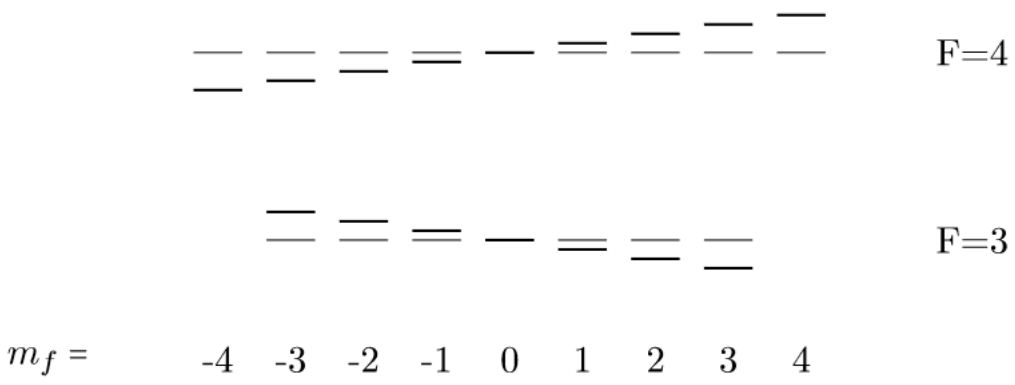

Figure 4.2: Energy level diagram for the ground state $6s^2S_{1/2}$ of caesium.

4.5 Interaction Hamiltonian

In this section we will explore the dynamics of our light-atom system. This will be an abridged version of the derivations which can be found in [1] and [11].
To start with we will write the interaction Hamiltonian between the probe laser and the atomic ensemble, which has been pump to the $|f = 4, m_f = 4\rangle$ state.

$$\hat{H}_{interaction} = \frac{-c\Gamma_0\lambda^2_{probe}}{16A\Delta\pi} \int_0^L \rho A \left(a_0\hat{\phi}(z,t) + a_1\hat{S}_z(z,t)\hat{F}_z(z,t) \right) dz, \tag{4.37}$$

where Γ_0 is the natural linewidth which arises form the spontaneous decay of the atoms in the exited state. Δ is the detuning of the probe laser, c is the speed of light in the vacuum, λ_{probe} is the wavelength of the probe, ρ is the density of atoms in vapor-cell, and L and A is the length and cross-section of the of the atomic ensemble respectively. We assume that the probe-laser is far detuned from the $6S_{1/2}, f = 4 \rightarrow 6P_{3/2}$ transition for the rest of the derivation. a_0 and a_1 are dimensionless parameter and at large detuning they will have the values $a_0 = 4$ and $a_1 = 1$. $\hat{S}_z(z,t)$ and $\hat{F}_z(z,t)$ are the stokes operator and the operator for the total angular momentum respectively. The stokes operator has the commutator relations describe in equation 4.26 and $\hat{F}_z(z,t)$ has the commutator relation

$$\left[\hat{F}_j(z,t), \hat{F}_k(z',t')\right] = \frac{i\delta(z-z')\epsilon_{jkl}}{\rho A}\hat{F}_l(z,t). \tag{4.38}$$

To find the dynamics of the system we will need to solve the equations of motion for the system. It can be shown that the Heisenberg equation for the stokes operators can be written as [11]

$$\left(\frac{\partial}{\partial t} + c\frac{\partial}{\partial z}\right)\hat{S}_j(z,t) = -i\left[\hat{S}_j(z,t), \hat{H}_{interaction}\right]. \tag{4.39}$$

To simplify this expression further we will not include retardation terms i.e. let the speed of light go to infinity and thereby ignoring the time derivative.

$$\frac{\partial}{\partial t}\hat{S}_j(z,t) = -i\left[\hat{S}_j(z,t), \hat{H}_{interaction}\right] \tag{4.40}$$

from this we get the equations of motion for the stokes operators

$$\frac{\partial}{\partial t}\hat{S}_x(z,t) = a_1\frac{\Gamma_0\lambda_{probe}^2\rho}{16\Delta\pi}\hat{S}_y(z,t)\hat{F}_z(z,t), \tag{4.41}$$

$$\frac{\partial}{\partial t}\hat{S}_y(z,t) = a_1\frac{\Gamma_0\lambda_{probe}^2\rho}{16\Delta\pi}\hat{S}_x(z,t)\hat{F}_z(z,t), \tag{4.42}$$

$$\frac{\partial}{\partial t}\hat{S}_x(z,t) = 0. \tag{4.43}$$

Given that we are working with a vapor-cell of length L means that the atoms are contained in a section of space which we define as $z = [0, L]$. Given this we now define the stokes operators $\hat{S}_i^{in}(t) = c\hat{S}_i(z=0,t)$ and $\hat{S}_i^{out}(t) = c\hat{S}_i(z=L,t)$. looking at the equations of motion we see that the solution for $\hat{S}_z$ is simply

$$\hat{S}_z^{in}(t) = \hat{S}_z^{out}(t) \tag{4.44}$$

For the two other stoke operators we have a set of first order coupled differential equations which have the solutions

$$\theta_F = \frac{-a_1\Gamma_0\lambda_{probe}^2\rho L}{32\pi\Delta}\hat{F}_z(z,t), \tag{4.45}$$

$$\hat{S}_x^{Out}(t) = \hat{S}_x^{in}(t)cos(2\theta_F) - \hat{S}_y^{in}(t)sin(2\theta_F), \tag{4.46}$$

$$\hat{S}_y^{Out}(t) = \hat{S}_y^{in}(t)cos(2\theta_F) + \hat{S}_x^{in}(t)sin(2\theta_F), \tag{4.47}$$

where θ_F is the Faraday angle. We can see from the equations that the polarization components in the x- and y-direction will be rotated around the z-axis as it passes through the atomic ensemble. The amount of rotation is dependent on several factors. Some of these factors, such as π, 32, and Γ_0, are beyond the control of us as mere mortal physicists while others are within our grasp.
ρ is dependent on the amount of caesium in vapor form inside the cell and can therefore be increased by increasing the temperature. L could be changed by using a different cell design. Δ and λ_{probe} are dependent on the specific settings of the probe laser and $\hat{F}_z(z,t)$ is dependent on the atomic state. The consideration of

maximizing $\hat{F}_z(z,t)$ will inform our decisions on pumping scheme which will be discussed in section 5.1. One change we may wish to make is the replacement of the atomic spin operators with the ensemble spin operators. We define this as

$$\frac{\partial}{\partial t}\hat{F}_x(z,t) = a_1 \frac{\Gamma_0 \lambda_{probe}^2 \rho}{16\Delta\pi} \hat{F}_y(z,t)\hat{S}_z(z,t), \tag{4.48}$$

$$\frac{\partial}{\partial t}\hat{F}_y(z,t) = a_1 \frac{\Gamma_0 \lambda_{probe}^2 \rho}{16\Delta\pi} \hat{F}_x(z,t)\hat{S}_z(z,t), \tag{4.49}$$

$$\frac{\partial}{\partial t}\hat{F}_z(z,t) = 0. \tag{4.50}$$

Given that $\hat{J}$ is just a linear combination of commuting $\hat{F}$, we may replace $\hat{F}$ with $\hat{J}$ and get the equations of motion for the total spin. This is only one component of the total equation of motion for the atomic spin and is the Faraday interaction.
Another effect on the atomic spin is the Zeeman effect as described in section 4.3, where the Hamilton is defined in equation 4.27 and the contribution to the equation of motion is in equation 4.31. The optical pumping as described in section 5.1 is applied along the x-axis and will therefore move the atoms to a spin-state along the x-axis. If we define the pumping-rate as R and $J_0 = 4N_a$ then we can write the equations of motion of the optical pumping as

$$\frac{\partial}{\partial t}\hat{J}_x(t) = R\left(J_0 - \hat{J}_x\right), \tag{4.51}$$

$$\frac{\partial}{\partial t}\hat{J}_y(t) = -R\hat{J}_y, \tag{4.52}$$

$$\frac{\partial}{\partial t}\hat{J}_x(t) = -R\hat{J}_z. \tag{4.53}$$

In our system there will of course also be effects that cause the spin components to decay. We will define two different factors: The spin lifetime, T_1, and the spin decoherence time T_2. as it is more convenient to define this in terms of rate then times we define $T_1 = \frac{1}{\Gamma_1}$ and $T_2 = \frac{1}{\Gamma_2}$. The decay will contribute to the equations of motion with:

$$\frac{\partial}{\partial t}\hat{J}_x(t) = -\Gamma_1\hat{J}_x, \tag{4.54}$$

$$\frac{\partial}{\partial t}\hat{J}_y(t) = -\Gamma_2\hat{J}_y, \tag{4.55}$$

$$\frac{\partial}{\partial t}\hat{J}_x(t) = -\Gamma_2\hat{J}_z. \tag{4.56}$$

If we combine all of these terms we get

$$\frac{\partial}{\partial t}\hat{J}_x(t) = \left(-\Gamma_1\hat{J}_x\right)_{decay} + \left(R\left(J_0 - \hat{J}_x\right)\right)_{pump} - \gamma\left(\hat{J}_z B_y - \hat{J}_y B_z\right)_{zeeman} + \left(-a\hat{S}_z^{in}\hat{J}_y\right)_{interaction}, \tag{4.57}$$

$$\frac{\partial}{\partial t}\hat{J}_y(t) = \left(-\Gamma_2\hat{J}_y\right)_{decay} + \left(-R\hat{J}_y\right)_{pump} - \gamma\left(\hat{J}_x B_z - \hat{J}_z B_x\right)_{zeeman} + \left(a\hat{S}_z^{in}\hat{J}_x\right)_{interaction}, \tag{4.58}$$

$$\frac{\partial}{\partial t}\hat{J}_x(t) = \left(-\Gamma_2\hat{J}_z\right)_{decay} + \left(-R\hat{J}_z\right)_{pump} - \gamma\left(\hat{J}_y B_x - \hat{J}_x B_y\right)_{zeeman}. \tag{4.59}$$

where $a = \frac{-a_1\Gamma_0\lambda_{probe}^2}{16\pi\Delta A}$. Now that we have the general expression for the equations of motion of the atomic spins and their effect on the light polarization we will move on to a few specific cases that will be relevant for understanding our experimental results.

4.6 Atoms and external magnetic field

4.6.1 Zero field

We will no look at the case of zero magnetic field and assuming that we polarize the probe beam along the x-axis. The chosen polarize mean that $\hat{S}_z^{in}$ will only have a non zero value because of noise. We assume this noise on $\hat{S}_z^{in}$ is negligible. From this we get the set of equations of motion

$$\frac{\partial}{\partial t}\hat{J}_x(t) = -\Gamma_1\hat{J}_x + R\left(J_0 - \hat{J}_x\right), \tag{4.60}$$

$$\frac{\partial}{\partial t}\hat{J}_y(t) = -\Gamma_2\hat{J}_y - R\hat{J}_y, \tag{4.61}$$

$$\frac{\partial}{\partial t}\hat{J}_x(t) = -\Gamma_2\hat{J}_z - R\hat{J}_z. \tag{4.62}$$

From these equations we see that the y- and z-component of the spin will just decay, and the rate of this will be different whether we pump or not. As for the $\hat{J}_x$ we will get into a steady state of

$$\hat{J}_x = \frac{RJ_0}{R+\Gamma_1}. \tag{4.63}$$

So for a well pumped ensemble defined by $R >> \Gamma_1$ we will have that $\hat{J}_x \approx J_0$. This is a coherent spin state.

4.6.2 Constant arbitrary field

For the case of an arbitrary constant magnetic field we will have the equations of motion:

$$\frac{\partial}{\partial t}\hat{J}_x(t) = \left(-\Gamma_1\hat{J}_x\right) + \left(R\left(J_0 - \hat{J}_x\right)\right) - \gamma\left(\hat{J}_zB_y - \hat{J}_yB_z\right), \tag{4.64}$$

$$\frac{\partial}{\partial t}\hat{J}_y(t) = \left(-\Gamma_2\hat{J}_y\right) + \left(-R\hat{J}_y\right) - \gamma\left(\hat{J}_xB_z - \hat{J}_zB_x\right), \tag{4.65}$$

$$\frac{\partial}{\partial t}\hat{J}_x(t) = \left(-\Gamma_2\hat{J}_z\right) + \left(-R\hat{J}_z\right) - \gamma\left(\hat{J}_yB_x - \hat{J}_xB_y\right). \tag{4.66}$$

To solve this rather complicated set of equations we will make that approximation that $\Gamma_1 = \Gamma_2$ which is equivalent to ignoring the depumping effect that elastic collisions will have on the atoms. If we define the quantities $|\mathbf{B}|^2 = \mathbf{B}\cdot\mathbf{B}$ which is the magnitude of the magnetic field squared, $\hat{J}_x^0 = \frac{RJ_0}{R+\Gamma_1}$ which is the steady state solution for the spin component along x in the case of no magnetic field as shown in equation4.63 and with the constant $\Delta B = \frac{R+\Gamma_1}{\gamma}$ we can write the solution as

$$\hat{J}_x = \hat{J}_x^0\frac{\Delta B^2 + B_x^2}{|\mathbf{B}|^2 + \Delta B^2}, \tag{4.67}$$

$$\hat{J}_y = \hat{J}_x^0\frac{B_xB_y - B_z\Delta B}{|\mathbf{B}|^2 + \Delta B^2}, \tag{4.68}$$

$$\hat{J}_z = \hat{J}_x^0 \frac{B_x B_z + B_y \Delta B}{|\mathbf{B}|^2 + \Delta B^2}. \tag{4.69}$$

Given that what we will read out from the atoms is related to the $\hat{J}_z$ component of the the spin. If we assume that we do a slow scan over the value of B_z then we can get a function in one variable, assuming the others are constant. We have to do a very slow scan as the assumption to derive these equation are that B_x, B_y, B_z are all constant. We see that in the case of $B_x = 0$ and $B_y \neq 0$ we will have a Lorentzian shape resulting from the B_z scan. The orientation of the Lorentzian will depend on the sign of B_y. A plot of this can be seen in figure 4.3

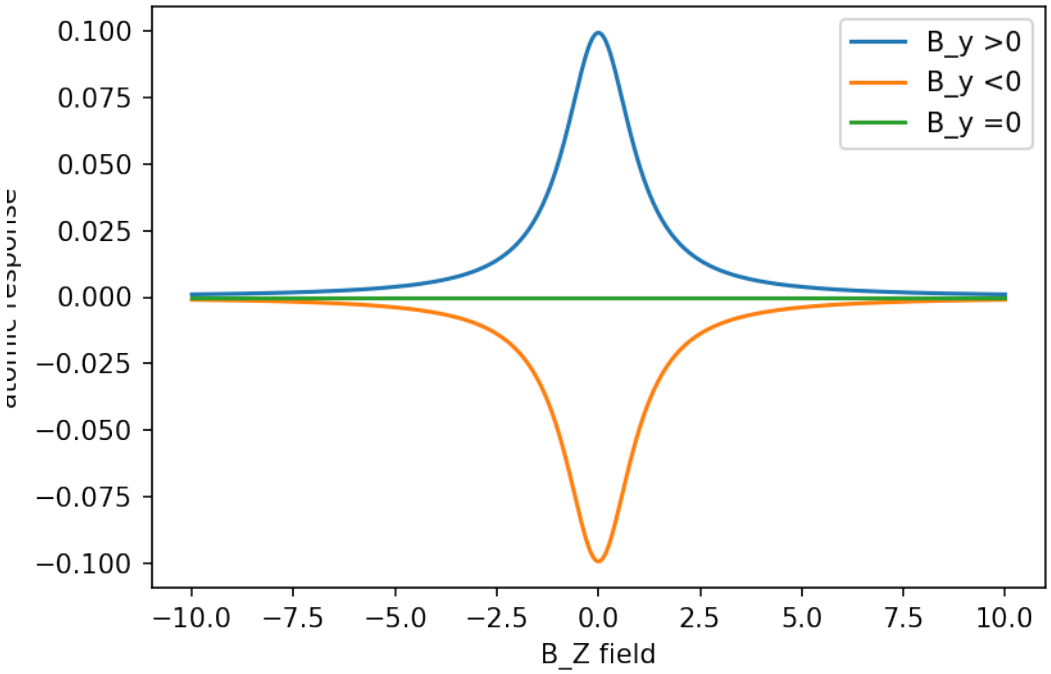

Figure 4.3: The expected atomic response as a function of B_z, for three cases of B_y.

If we were to do the same again, just with $B_x \neq 0$ and $B_y = 0$ we can see from equation 4.69 that we will end up with a dispersive lineshape instead of a Lorentzian one. Changing the sign of the non-zero field component will mirror the lineshape around the x-axis in the plot.

4.6.3 Arbitrary time varying field along the y-axis

Without going into much detail, we get from [1] that for an arbitrary time varying field in the y-direction the expectation value of the output stokes operator in the

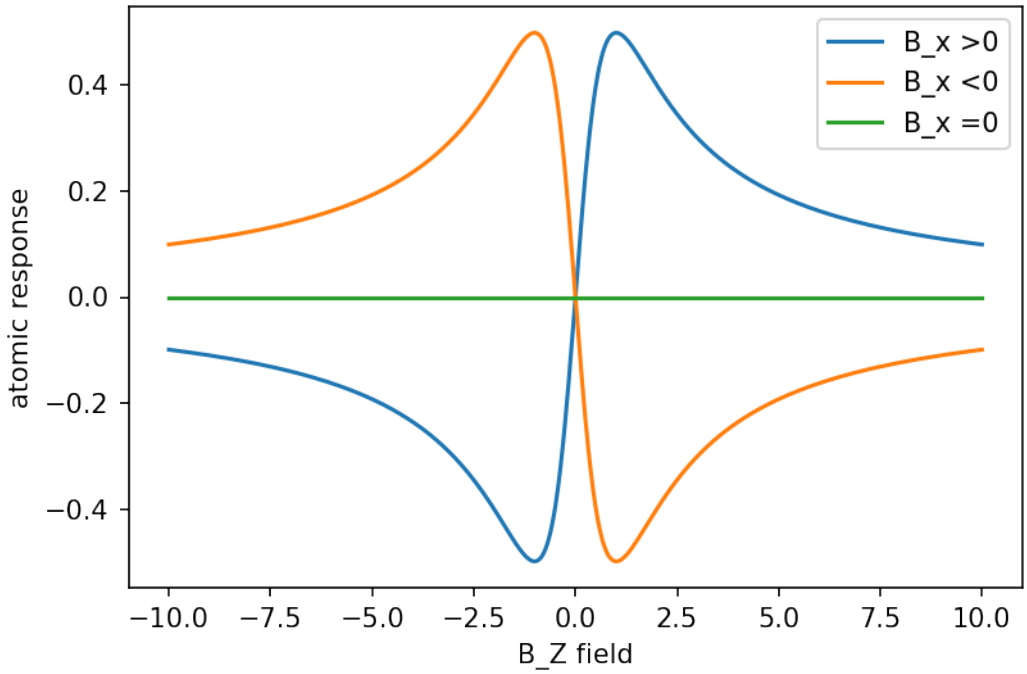

Figure 4.4: The expected atomic response as a function of B_z, for three cases of B_x.

y-polarization may be written as

$$\left\langle \hat{S}_y^{out} \right\rangle (t) = -aS_x\gamma J_x \int_{t'=-\infty}^{t} B_y(t') \left(cos(\omega_L t)cos(\omega_L t') + sin(\omega_L t)sin(\omega_L t')\right) e^{-(R+\Gamma_2)(t-t')} dt' \tag{4.70}$$

$$= -aS_x\gamma J_x \int_0^{\infty} B_y(t'\tau) \left(cos(\omega_L \tau)\right) e^{-(R+\Gamma_2)\tau} d\tau' \tag{4.71}$$

$$= \int_0^{\infty} B_y(t'-\tau)\kappa(\tau) d\tau', \tag{4.72}$$

where we define $\tau = t - t'$ and $\kappa(\tau) = cos(\omega_L\tau)e^{-(R+\Gamma_2)\tau}$. $\kappa(\tau)$ is what we call the kernel or impulse response and we see that the magnetometer signal is the result of a convolution between the kernel and the time varying magnetic signal. From this we also see that the kernel will be dependent on the transverse field that the magnetometer is subjected to given that it is dependent on the Larmor frequency ω_L. This also gives us the option of finding the strength of the transverse magnetic field by either fitting to the kernel or looking at the Fourier transform to determine ω_L. The kernel will also be dependent on the laser powers as the exponential decay depends on Γ_2. So we will need to remeasure the kernel for each set of parameters under which we wish to test the magnetometer.

5 Experimental method

5.1 Pumping scheme

In the experiment we will use a laser to interact with the atom spin of the caesium atoms present in our vapor-cell. We do this to gain information about the magnetic field that permeates the vapor cell. To this end we would like to prepare our atomic ensemble in a spin state where as many of the atoms as possible have the same spin. To get the best result we would like to put the atoms into a state with a large value of $|m_f|$ as this will interact the strongest with a given magnetic field. The state should also be one with a reasonable lifetime so the atoms don't decay immediately when we stop pumping.
The two best candidates for this is the $|f = 4, m_f = 4\rangle$ and $|f = 4, m_f = -4\rangle$ as they have a large m_f and a long lifetime. We make the choice of using the $|f = 4, m_f = 4\rangle$ state. Now that we have chosen a desired atomic state we need to transfer as many atoms to this state as possible. To accomplish this we use optical pumping.
When we are doing optical pumping, we are limited in what transitions we can drive. The factors limiting us are called the selection rules, and they arise from the fact that we need to have both energy and momentum conservation, in our process. To ensure that there is energy conservation we will need to match the wavelength of the laser to the energy difference between the two levels in the transition. The energy of a photon is $E = \hbar\omega$ where $\hbar$ is the Planck constant and ω is the angular frequency of the photon.
From the conservation of momentum we can get a series of restriction on the difference between the quantum numbers of the two states we are transitioning between[4].

$$\Delta l = \pm 1 \tag{5.1}$$

$$\Delta s = 0 \tag{5.2}$$

$$\Delta j = 0, \pm 1 \tag{5.3}$$

$$\Delta f = 0, \pm 1 \tag{5.4}$$

$$\Delta m_f = 0, \pm 1 \tag{5.5}$$

The allowed difference in the m_f number is determined by the polarisation of the light. σ_+ drives a $\Delta m_f = 1$, σ_- drives a $\Delta m_f = -1$, and linear polarisation drives a $\Delta m_f = 0$.
Due to all these restrictions we will use two lasers which we call the pump and the re-pump laser. The re-pump laser is locked on the $F = 3 \rightarrow F' = 2, 3$ crossover transition and have a right hand circular polarisation. This will make it resonant with the D_2 line between the $6s^2S_{\frac{1}{2}}, f = 3$ state and the $6p^2P_{\frac{3}{2}}, f = 4$ state.
The pump laser will have a wavelength of 852 [nm] and will also have a right hand circular polarisation. This will make it resonant with the D_1 line between the $6s^2S_{\frac{1}{2}}, f = 4$ state and the $6p^2P_{\frac{1}{2}}, f = 4$ state.

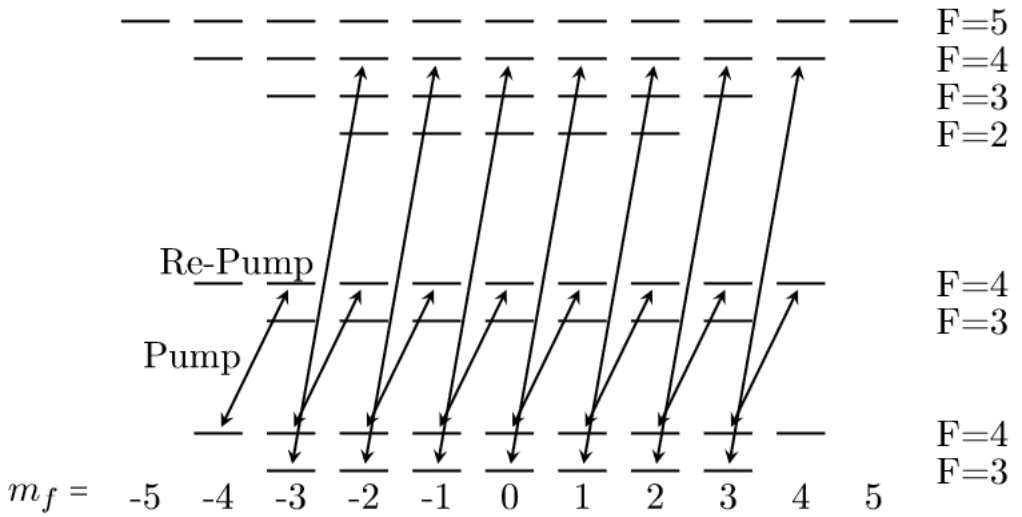

Figure 5.1: The energy level diagram of the valance electron of caesium-133 with transitions driven by the pump and repump laser indicated. This figure shows levels $S_{1/2}$, $P_{1/2}$ and $P_{3/2}$ (from bottom to top)

As the spontaneous decay of the electron may happen along any of the allowed transitions, this will result in the electron being shifted to the right in our energy level diagram. This will continue until it decays into the $|F = 4, m_f = 4\rangle$ in the ground state. The pump does not drive it out of $|F = 4, m_f = 4\rangle$ since there is no $|F = 4', m_f = 5'\rangle$ state in the $P_{1/2}$ manifold.

5.2 Magnetometer layout and design

Throughout this project we will be dealing with a magnetometer that is built in a 3D-printed box consisting of two parts: A lower shell where all the components will be mounted, and a lid. The lid will be put on as the last step of assembly to ensure that none of the components are accidentally moved. The magnetometer layout is designed by Michael Zugenmaier(Post.Doc) and is based on previous experiences gathered Hans Chr. Stærkind(Ph.D) in his work with designing 3D printed optical sensors for MRI measurements. The internal setup of the optical elements is based on the setup used to get the measurements in [10]. The primary goal of this project is to re-create the measurements of [10] with a 3D printed, miniaturized, fiber coupled magnetometer.
A labeled picture can be seen in figure 5.2, and more pictures of the magnetometer can be found in appendix B, and a diagram of the optical setup can be seen in figure 5.3. I will refer to these throughout the explanation of the setup.

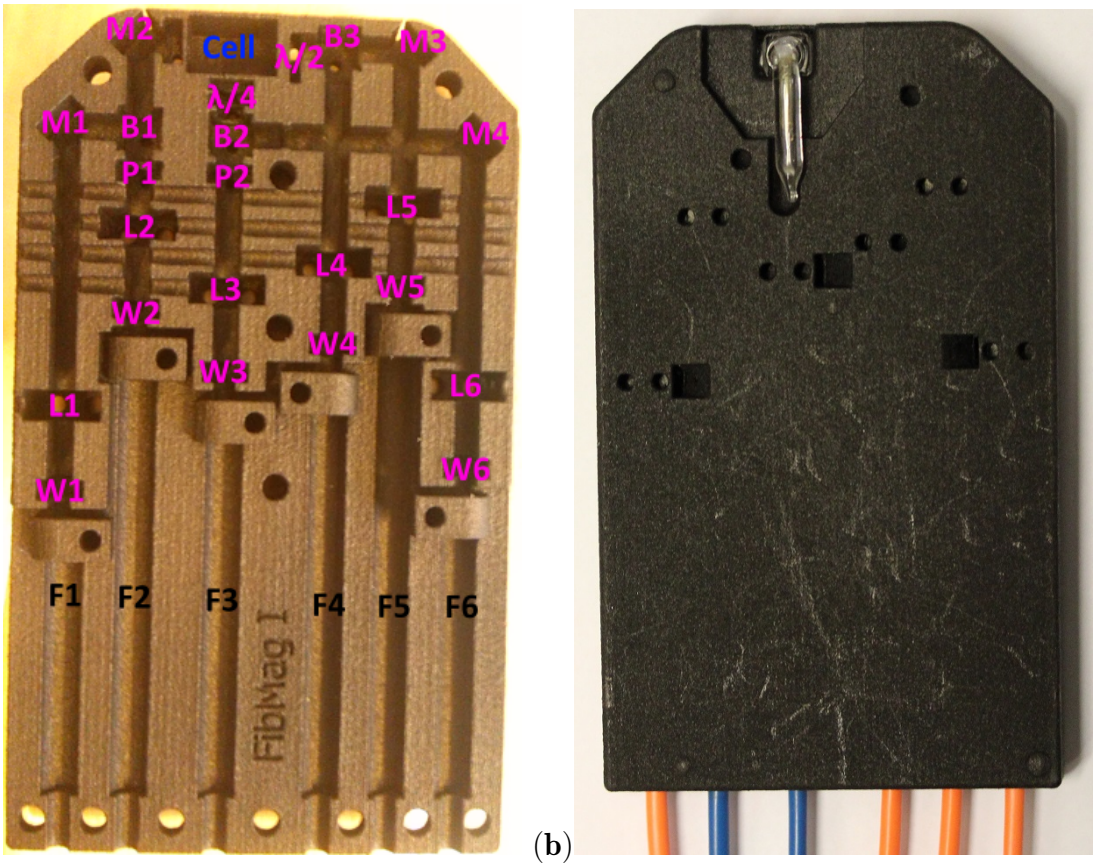

(**a**) (**b**)

Figure 5.2: **(a)** Picture of the magnetometer with labels **(b)** Closed magnetometer as seen from above

In the magnetometer there are 6 fibers for in/out coupling. F1 is a multi-mode fiber that out-couples 10% of the probe so that we can monitor the total power and its stability. Later this was also used to power stabilise the probe - even though it was not intended in the design, it worked quite well. F2 is the input coupling for the probe laser, this fiber is a single mode polarisation maintaining fiber. F3

is the input coupling for the pump and re-pump lasers. This fiber is also single mode polarization maintaining. F4 and F5 are the two output for the balanced detection. Both of these are multi-mode fibers. F6 is for monitoring the pump/ re-pump with 10% of the total power of these lasers' output. Out of the 6 fibers in the magnetometer, only 4 of the are strictly necessary for the basic functioning of the magnetometer them being F2,F3,F4, and F5.

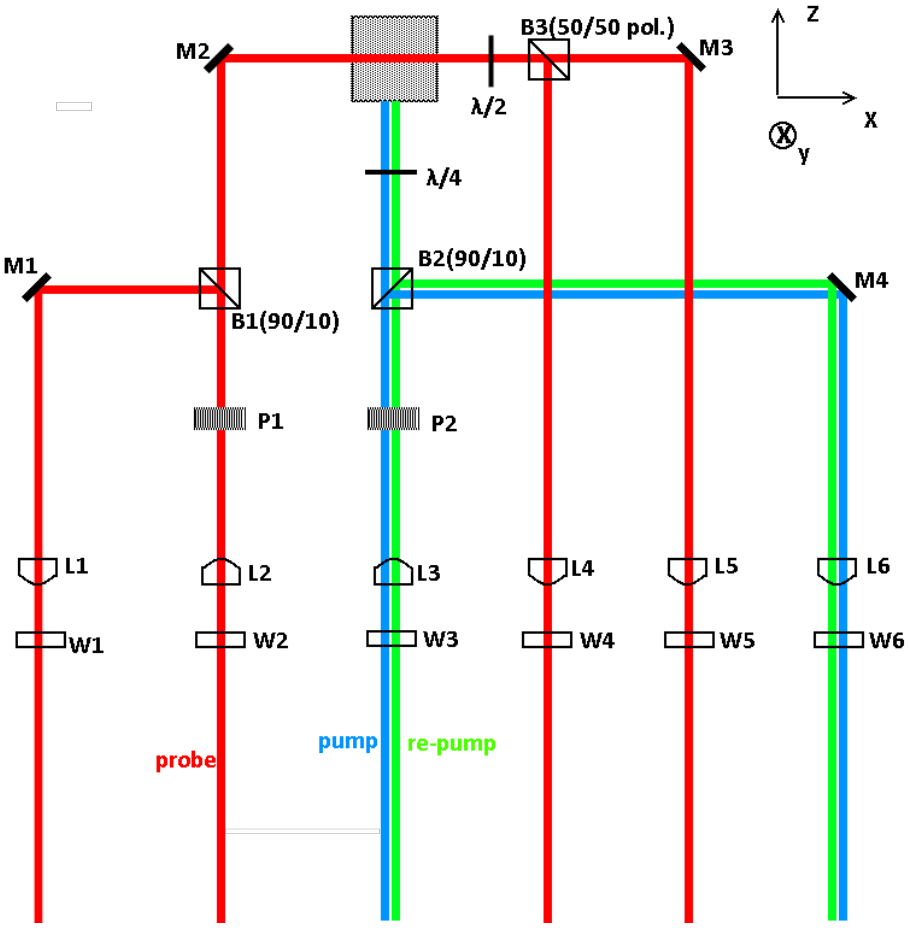

Figure 5.3: Optical diagram of the magnetometer.

All the fibers are connected to the magnetometer by pushing the end up against a "window", applying index matching fluid, and clamping it down with the clamp that is part of the nylon construction of the magnetometer, and a nylon screw. The windows are coated with an anti reflective coating to prevent back-scattering. The index matching fluid was added to prevent possible fiber modes to interfere with the operation of the magnetometer.
In the path of both the probe and the pump/re-pump we have placed a polarizer, even though the fibers we use to input the lasers are polarization maintaining. This is done to ensure that we only have the correct linear polarization before the laser interacts with other components and the atoms. In the idealised case these should not be necessary, but there is no harm done by adding them, and the real world is rarely an idealised case. Just before getting to the cell, the pump/re-pump passes though a 90/10 beamsplitter, and a the 90% goes though a $\lambda/4$ wave-plate and into

the atomic ensemble. The 10% of the power is output for monitoring. The $\lambda/4$ waveplate gives the pump/re-pump the right hand circular polarization that it needs to work in the pumping scheme as defined in section 5.1. After the pump/re-pump passes though the cell, it terminates at the magnetometer wall and should not have any back reflections as it is made from nylon.
After the probe passes though the atomic ensemble it goes through a $\lambda/2$ waveplate which will turn the linear polarisation by 45^o. It is then incident on a polarising beamsplitter with it's polarisation axis along the y-axis. So in the case where the atomic ensemble doesn't change the polarisation of the probe, half of the light will go down each arm to the fibers F4 and F5 and, assuming identical output coupling efficiency, equal amounts of light will hit both of the photodiodes in the balanced photo detector.
The lenses in each of the fiber arms have one of two purposes. For the input fibers it is to collimate the laser beam after it exits the fiber as the laser beam coming out of the fiber diverges. For the outputs the lens focuses the light so the most of it hits the fiber core and is thereby coupled out of the magnetometer. The lenses are also used for alignment of the laser-beams.

5.2.1 Magnetometer assembly

To construct the magnetometer, several different optical components need to be placed and fixed in position inside the 3D-printed shell. After consulting with Hans Chr. Stærkind, we were provided with his suggested process of assembly. As the two magnetometers are only of similar but not identical designs, we made some modifications to the process. We will now briefly go through the process of assembling the magnetometer.
All the lenses in the magnetometer are identical. They are circular with a flat side and a convex side and as such will fit not well into the rectangular slots in the magnetometer shell. The lenses are therefore mounted, by the use of glue, in rectangular plastic lens-holders made for this purpose. Due to the, by quantum optics standards, large manufacturing tolerance of 3D printed items, the lensholders are selected such that they are slightly too large for the lens slots and are thereafter filled, by hand, such that they are just able to be pushed into the slots. This ensures that the lenses position can be adjusted if we deliberately push on them, but they will not move once the magnetometer is closed, unless we use the alignment holes. The fibers are simply clamped in place using the brace that is built into the shell, and tension is applied by a nylon screw.
The rest of the components are fixed in place using epoxy. When inserting these elements, a visible laser is sent through the fiber and into the magnetometer to help the alignment of the elements. The elements are then inserted one by one starting with the first in the beam-path, either probe or pump/repump, and then we work our way forward though the beam-path. When all the elements have been inserted, the magnetometer is closed, and final alignment of the lenses will be done. This alignment is done by inserting rods in the small grooves that can be seen connecting the side of the lens slots to the edges in figure 5.2**a**. Where there is no groove, the diagonal slots in the lid are used, which can be seen in figure 5.2**b**. The two holes next to the slots are mirrored on the bottom and are used to adjust the lenses posi-

tion up or down after the magnetometer have been closed. For the fine alignment of the lenses after the magnetometer have been closed a special tool was designed and constructed. Pictures and technical scale drawings can be found in appendix A.

5.3 Calibrating magnetic field

In the experiments there are several different kinds of magnetic fields that we will need to determine or cancel. To be able to do this we will do a short overview of different methods to be able to cancel transverse magnetic field and determine the size of induced RF fields and induced DC fields.

5.3.1 DC transverse field cancellation

As we saw in section 4.6.2 we can determine the transverse field by looking at the line-shape of the atomic response as we scan over B_z. Of course in general the field is going to be some combination of transverse x- and y-field, which will result in that the lineshape we will see on the scope not being a "pure" Lorentzian or dispersive shape. The method that we settled on for canceling the field is that we simply pick what seems to be the dominating component and then cancel that first. Let's say that the lineshape is mostly dispersive, then we will tune the current on our B_x coil until we have a mostly Lorentzian shape. Then we go on to tune the B_y current until we are either almost flat or the feature we see is either mostly Lorentzian again or just a small residual. If it is Lorentzian we go back to tuning the B_x current. We keep switching back and tuning the current until we have an almost flat line. We would of course like for it to be completely flat, but we will most likely have a small residual feature left that is neither Lorentzian nor dispersive. Looking at figure 5.4 we see a trace of badly calibrated B_x cancellation along with a good trace of the well canceled field. In figure 5.5 we see the case of a badly canceled B_y field along with the same, well canceled trace. We have in general found that it is necessary to perform this cancellation every day before we start measuring, and also after every time we degauss.

5.3.2 AC-RF field strength determination

To find the sensitivity of the magnetometer in the Radio frequency(RF) domain we need to be able to apply an RF field of known magnitude. One way to estimate the strength of the applied field is to use the physics of the AC Faraday effect. For the full theoretical explanation please see [16]

The conceptual explanation is that if we have a macroscopic spin state that starts off in the state being completely aligned along an applied B-field in the x-direction, and we then also apply an RF magnetic field along the z-axis, then we may write the Hamiltonian of the system as

$$\hat{H} = \omega_0 \hat{F}_x + A\hat{F}_z cos(\omega_d t), \tag{5.6}$$

where the $\hat{F}_i$ operator is the operator of the spin in the i direction, $A = 2\pi\gamma B_{rf}$ is the coupling Rabi frequency with field strength B_{rf}, and the gyro-magnetic ration for

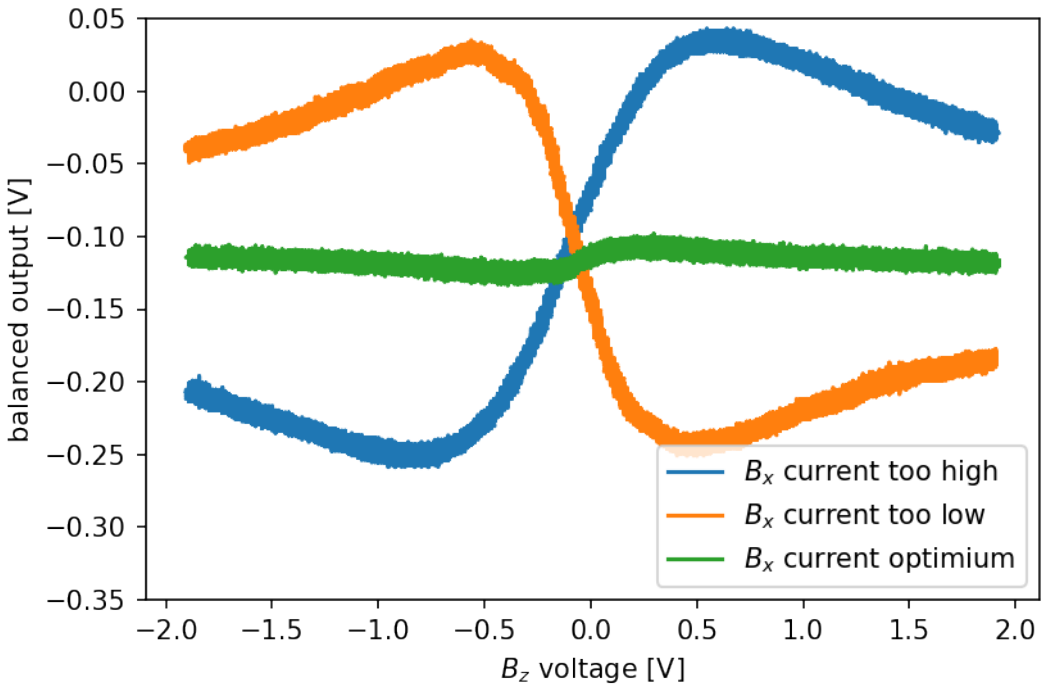

Figure 5.4: The atomic response for different values of B_x as a function over B_z. The blue line is for a too large current on the B_x coil, orange is to little current and the green trace is the value of B_x current that gives us the smallest feature.

caesium $\gamma = 350[\frac{kHz}{G}]$. One may find the equations of motion for this system by going to the Heisenberg picture and applying the Heisenberg equation to the three spin operators $\{\hat{F}_x, \hat{F}_y, \hat{F}_z\}$. Solving this system for the initial conditions $(F_x, F_y, F_z) = (J, 0, 0)$ we get

$$\frac{F_x(t)}{J} = \frac{e^{-\Gamma t}}{\widetilde{A}^2}\left[cos\left(\frac{\widetilde{A}t}{2}\right)A^2 + 4\Delta^2\right], \tag{5.7}$$

$$\frac{F_y(t)}{J} = \frac{Ae^{-\Gamma t}}{\widetilde{A}} sin\left(\frac{\widetilde{A}t}{2}\right), \tag{5.8}$$

$$\frac{F_z(t)}{J} = \frac{4A\Delta e^{-\Gamma t}}{\widetilde{A}^2} sin^2\left(\frac{\widetilde{A}t}{4}\right). \tag{5.9}$$

From this we can see that

$$F_y \propto sin\left(\frac{At}{2}\right), \tag{5.10}$$

so if we measure F_z and find the time it takes to drive a π transition, then we can calculate B_{rf} by

$$B_{RF} = \frac{A}{2\pi\gamma} = \frac{1}{t_\pi \gamma}. \tag{5.11}$$

Two plots at different B_{RF} can be seen in figure 5.6.

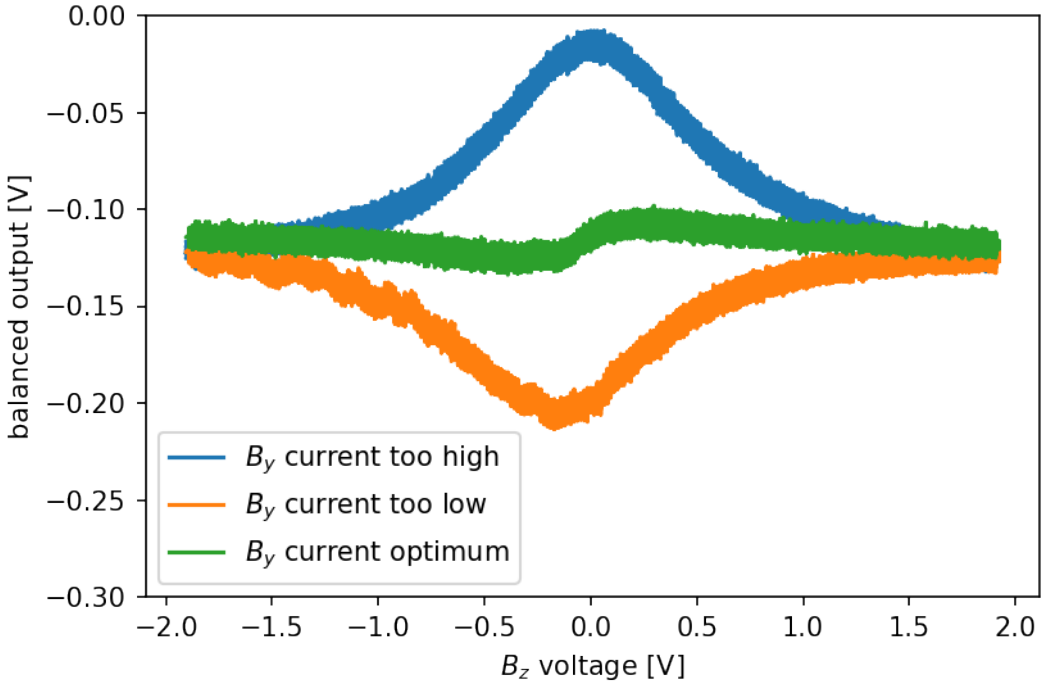

Figure 5.5: The atomic response for different values of B_y as a function over B_z. The blue line is for a too large current on the B_y coil, orange is to little current and the green trace is the value of B_y current that gives us the smallest feature.

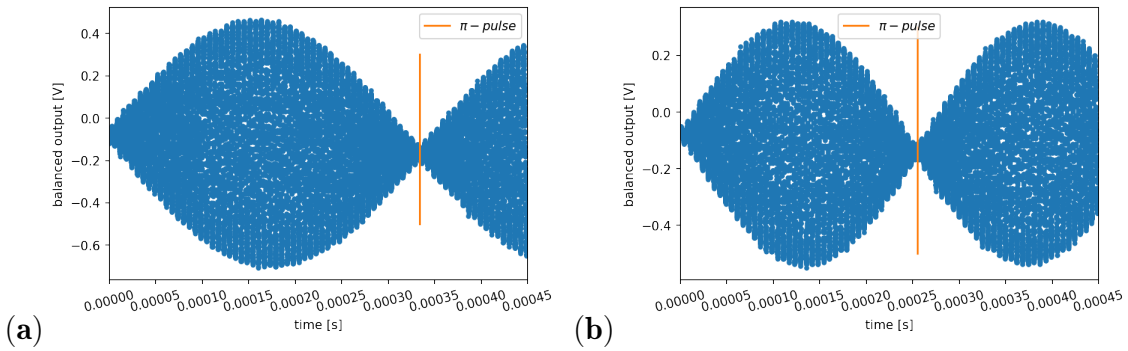

Figure 5.6: Plots of the atomic response to RF excitement. Both are taken at the same Larmor frequency but with different RF field strength. **(a)** plot of the driven transition with $20[V_{pp}]$ on the RF coil with a $1[k\Omega]$ resistor in series. The time to drive a π transition is $255 \cdot 10^{-6}[s]$. **(b)** Plot of the driven transition with $15[V_{pp}]$ on the RF coil with a $1[k\Omega]$ resistor in series. The time to drive a π-transition is $334 \cdot 10^{-6}[s]$

If we apply this procedure for several different RF drive voltages, then we get a, hopefully linear, relationship that we can use to find the B_{RF} field strength for any given drive voltage. If there is no resonances in the circuit, then we would expect that there is a linear relationship between the applied voltage and the RF-

field strength because of Ohm's law and the expected field generated from a pair of Helmholtz coils [5].

$$I = \frac{V}{R}, \tag{5.12}$$

$$B = \left(\frac{4}{5}\right)^{3/2} \frac{\mu_0 N I}{r}, \tag{5.13}$$

where V is the applied voltage, R is the resistance, N is the number of windings in the Helmholtz coils, r is the radius of the Helmholtz coils, and μ_0 is the vacuum permeability. In figure 5.7 we see the magnetic field calculated from the estimated

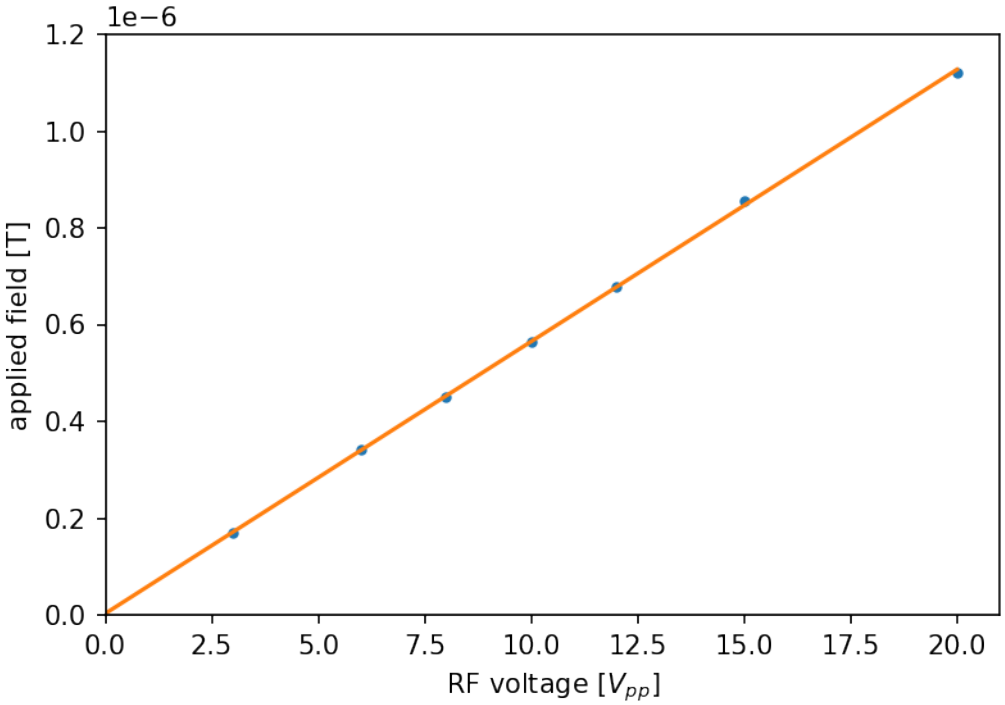

Figure 5.7: The relation between the input RF voltage and the estimated B_{RF} field strength with a straight line fit. $f(x) = 5.62 \cdot 10^{-8}x + 2.69 \cdot 10^{-9}$

t_π time in relation the the drive voltage applied to the RF coil. By visual inspection the relationship seem quite linear with very little error. If one wanted to reduce the error even further, one may realise that the main source of error in this estimation method comes from deciding on the exact place of the minimum, such as the ones indicated with the orange lines in figure 5.7. This error does not change whether we are finding the t_π time or the $t_{N\cdot\pi}$ time. We can therefore drive the atomic ensemble for a few more cycles and make the error go down with $\frac{1}{N}$, though the total $t_{N\cdot\pi}$ should be much smaller than the t_2 of the system.

5.3.3 DC field strength determination

The field strength found in the previous section was for a RF field. We also need a method to find the field strength of a DC field. There are several ways in which

we can do this, but all of them will estimate the Larmor frequency and then use equation 6.2 to determine the field strength. The first method we could employ is to simply us the RF coil to excite the atoms with broadband noise. If we then measure the atomic response and look at the Fourier transform, we should find a peak at the Larmor frequency.
If we input a sine wave on the RF coil instead of broadband noise, we will only excite the atoms if the frequency of the sine wave is close to the Larmor frequency. The largest response will be when $\omega_{RF} = \omega_{Larmor}$. So by simply observing the response on the scope, we can find the frequency that gives the largest amplitude response.
The last method is to use the kernel as found in the theory section: $\kappa(\tau) = cos(\omega_L \tau) e^{-(R+\Gamma_2)\tau}$. With this we can either do a fit to find ω_L or a Fourier transform.

6 Results

We will now have a look at how we can use the magnetometer to measure the strength of a magnetic field. We will have a look at three different modes of operation: Free induction decay(FID), RF , and continuous DC. The FID magnetometer technique is measuring the bias field in the DC/low frequency domain. But first we will determine the coherence time of the vapor-cell while it is inside our magnetometer to ensure that it is working as expected.

6.1 $\mathbf{T}_2$

To determine the coherence time of the collective atomic spin-state in our vapor-cell, we measure the decay of the projection of the collective spin on the axis of the probe light propagation direction. We do this by first applying the pumping scheme as described in section 5.1. When we have reached a state where most atoms are in the $F = 4, m_F = 4$ state, we apply a sinusoidal RF excitation that is perpendicular to the optical plane. The frequency of the excitation is equal to the Larmor frequency of the atoms at the given bias field.
This RF excitation will cause the atomic spin to start precessing around the axis defined by the magnetic bias field. In this case the bias field is along the axis of the magnetic shield, which is the x-direction. Once we have a sufficiently large projection, which usually only takes a few oscillations of the on resonance RF field, the RF field is turned off, and the decay of the atomic spin state can be observed through the far detuned and linearly polarized probing of the probe laser, as its polarization is changed by the Faraday rotation caused by the atoms as described in section 4.5. The pump laser is also turned off to eliminate the R term in the exponential decay as seen in section 4.5.
After we have measured the signal, as can be seen in figure 6.1**a**, we fit it with the function similar to the one defined in eq. 6.1. One change to the function is that $k = 0$ as we AC couple the scope for this measurement, and we therefore will not have an offset. As we can see in figure 6.1**b**, our fit(orange) is in good agreement with the data(blue). From the fit we extract the decay-time, $T_2 = 17[ms]$. As described in section 4.5, $T_2 = \frac{1}{\Gamma_2}$.
This is in good accordance with the data collected on the vapor-cell before inserting it into the magnetometer, where the T_2 was measured to be around $\approx 20[ms]$ for very low laser powers. Given that we have about the same performance of the vapor cell in the magnetometer as we did in the test before inserting it into the magnetometer, we conclude that the magnetometer is working as intended in regards to the spin coherence, and we will therefore proceed to test the sensor's performance as a magnetometer.

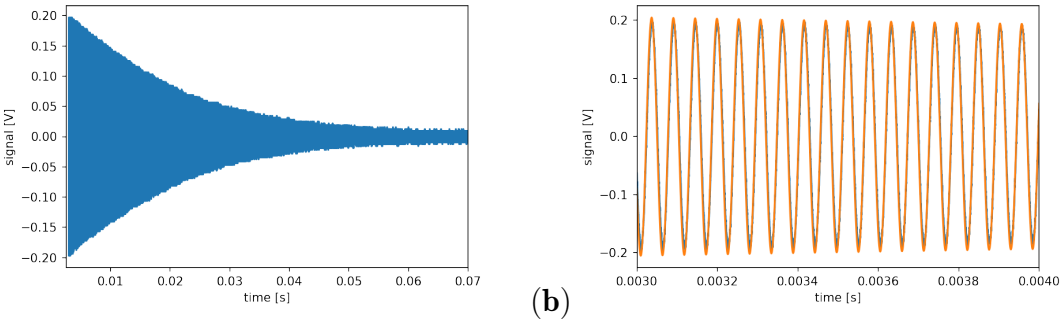

(**a**) (**b**)

Figure 6.1: **(a)** Decay of the atomic spin. **(b)** zoom-in on the decay of the atomic spin. The blue is the data, and the orange is the fit. the T_2 is approximately 17 ms

6.2 Free induction decay(FID) magnetometer

Taking inspiration from the paper by D. Hunter et. al. [6], we used the free induction decay of the atomic spin to determine the magnetic field. Contrary to the other modes of operation discussed in this thesis, this is a pulsed method, where each pulse can be split into three phases. The three phases can be seen on figure 6.2**b**. Before the measurement starts, the pumping scheme from section 5.1 is applied to prepare the atomic state. After the atoms are well pumped into the $|F = 4, m_F = 4\rangle$ manifold, we apply a few oscillations of RF excitation at the Larmor frequency. This is the phase indicated with a 1 in the top of fig6.2**b**. After this, the pump laser is blocked and the RF excitation is stopped. The free induction decay is observed with the probe for a time significantly longer than $1/f_{Larmor}$, as we need to fit a sine wave to this later. This is the phase indicated with a 2 and the red bar in figure 6.2**b**. In phase 3 the pump is unblocked and the atoms are again pumped into the $|F = 4, m_F = 4\rangle$ manifold, whereafter the process starts over again. In figure 6.2 we can clearly see the difference in decay rate between having the pump laser on or off. This measurement is repeated back to back. A cutout of a data-trace can be seen in fig 6.2**a**. What we end up with is a trace that contains 160 pulses in 1 second. From the data we select the 160 regions of free induction decay with no pump and fit the function we defined in equation 6.1.

$$g(t) = A \cdot cos\left(2\pi \cdot f \cdot t + \phi\right) e^{(-1/T_2)t} + k, \tag{6.1}$$

where A is the amplitude, f is the frequency in [Hz], ϕ is the phase, T_2 is the coherence time, and k is an offset as the input to the balanced photo-diode may not be perfectly balanced in all cases.
We will now test the magnetometers performance at a few different frequencies in this mode of operation. This was both intended as a means to compensate for possible peaks in the noise and to ensure that we have a wideband magnetometer. As it turns out, only one of the tested frequencies was working as intended in the end.

6.2.1 FID at 5.3 kHz & 25 kHz Larmor frequency

Looking at figure 6.2**a**, we see three and a bit of the consecutive pulses. We can clearly see the three phases, RF-excitation, no-pump decay, and pumping to $F = 4, m_F = 4$, as described in section 6.2. In figure 6.2**b** we see the start selection of the fitted portion marked by the orange star. The end of the fit selection is marked by the green star. As the only quantity in the fit that we are interested in at the moment is the frequency in the FID phase (phase 2), the end of the selection is deliberately a bit short so that we do not get any of the of the pumping phase included in our fit. We exclude phase three from the fit because the Larmor Frequency will will be shifted due to the Stark shift caused by the pump and repump. Looking at figure 6.3**a**, we see that the fit (orange) is in good agreement with the data (blue). This is the case for all the fits of the free induction decay we make in this section.

One data file is in total one second long and contains 160 individual FID's which are evenly spaced in time. Each of these are fitted, and the fitted Larmor frequencies are shown in figure 6.3**b**. It is clear to see that the Larmor frequency is not stable, but what we see are not random fluctuations either, as there is a clear pattern. Given the very poor stability of the Larmor frequency, it does not make sense to continue with the data-analysis of this data file to find the noise floor. The reason for this pattern in the Larmor frequency is not known with complete certainty, but it is highly suspected that it is the result of the current-supply not being able to provide a stable current at the given setting. This is suspected for 2 reasons:

1. Looking at the data in 6.3**b**, it seem that the Larmor frequency is always "aiming" at a value in the range of 5345 Hz but keeps overshooting and correcting.

2. This pattern disappeared when we increased the current that the power-supply had to output, confirming that the problem has something to do with the power supply.

The strange feature is still somewhat present when the current is increased such that we have a Larmor frequency of $\approx 25[kHz]$, but it goes away when the Larmor frequency is $\approx 51[kHz]$, and we will therefore shift our focus to the $\approx 51[kHz]$ case.

6.2.2 FID at 51 kHz

We will go through the same process with the $51[kHz]$ Larmor frequency data as we did with the $5.3[kHz]$ Larmor frequency data. Looking at figure B.2**a**, we again see the three phases which are present in all the individual pulses: Excitation, free induction decay (with no pump), and pumping, which is technically still free induction decay but now with the pump added, which will increase the decay rate. The extra pattern that seems to be in the data is most likely an artefact of the sampling rate of the scope and the Larmor frequency.
Looking at figure 6.4**a**, we see the fit of the decaying sine-wave (orange) overlaid on the data (blue). We see that the decay seem slightly more linear than exponential, but as stated before, we are in the end only interested in extracting the Larmor

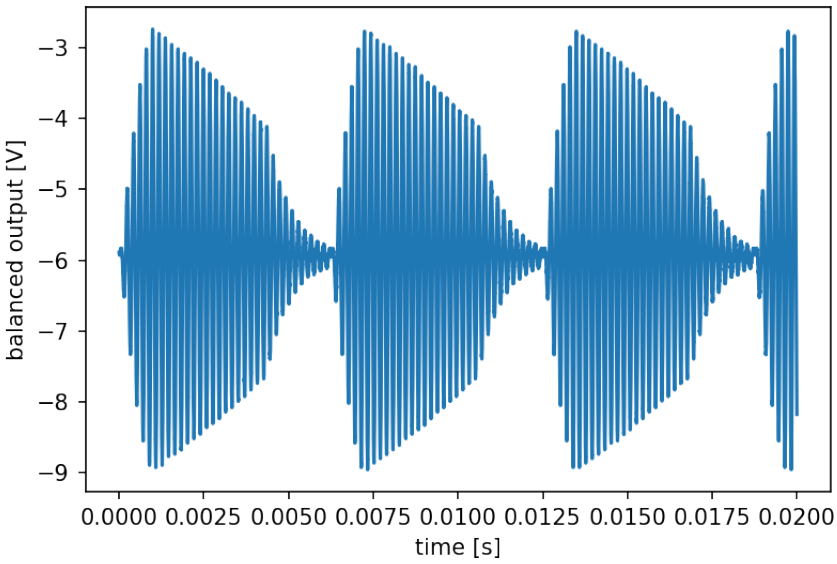

(**a**)

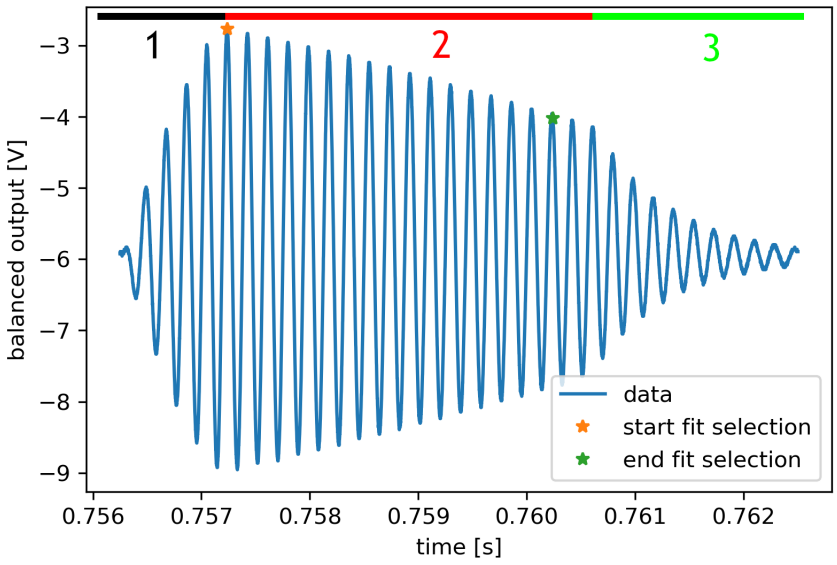

(**b**)

Figure 6.2: **(a)** Pulse-train at a repetition rate of 160 Hz and a Larmor frequency of approx. 5.3 kHz. **(b)** Zoom-in on a single drive-decay-pump cycle.

frequency. If we look at figure 6.4**b**, we see that the fit has good agreement with the data in terms of frequency and decay over the shown range.

In figure B.2**a** we see that the three phases of the pulse behave the same at a Larmor frequency of $51[kHz]$ as it did at a Larmor frequency of $5.3[kHz]$.
We see in figure B.2**b** that we now have a Larmor frequency that only varies by around $\pm 0.5[Hz]$. The systematic nature of the variation also seems to be gone, so we can continue the data analysis with at this frequency to find the noise floor.
From the 160 fitted Larmor frequencies we can calculate the strength of the bias

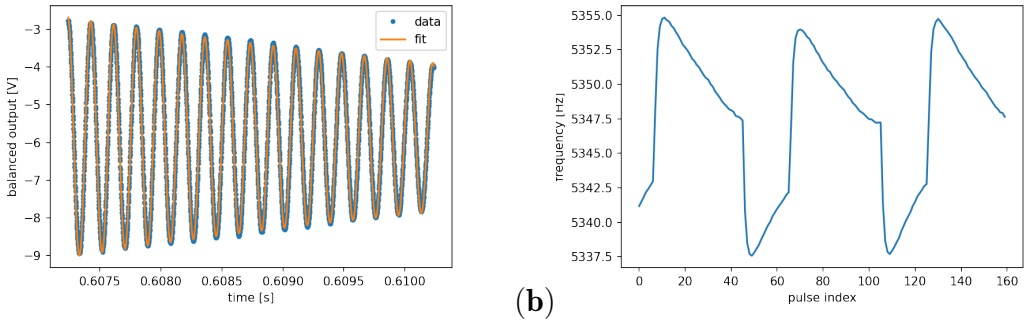

(**a**) (**b**)

Figure 6.3: **(a)** Fit to the spin decay. **(b)** The 160 frequencies found by fitting to the pulses. As we can see the frequency is not stable.

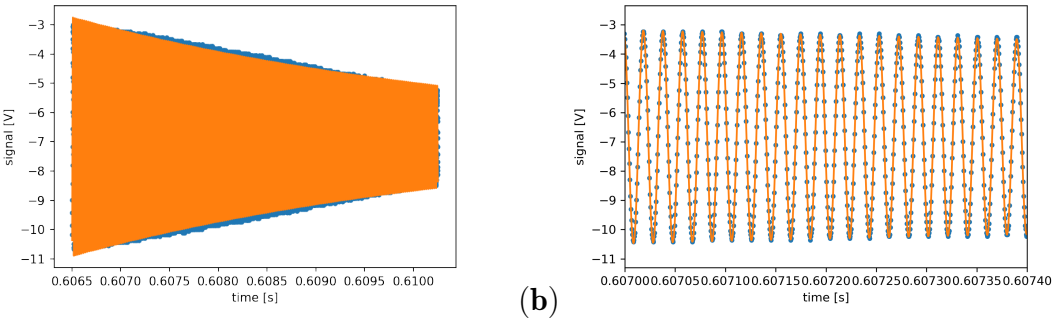

(**a**) (**b**)

Figure 6.4: **(a)** Fit to the spin decay for a Larmor freq. of 50 kHz. **(b)** Zoom-in on 50 kHz fit.

magnetic field with the relation:

$$\omega = \gamma B, \tag{6.2}$$

where γ is the gyromagnetic ratio. for caesium this is $\gamma = 3.5[Hz/nT]$.

Once we have found the strength of the magnetic field, we calculate the power spectral density (PSD) of the fitted Larmor frequencies. The PSD can be defined as

$$power = \int_0^\infty PSD d\nu, \tag{6.3}$$

so calculating the PSD will give you a function over how much power your signal has within each frequency slice $d\nu$. Given that we need a signal-to-noise ratio over 1 for detection, we may calculate the PSD of the signal, which will give us the noise floor of the sensitivity in this mode of operation and under the given conditions of magnetic shielding, power-supply used, laser powers, etc. Taking the square root of this will give the Root Spectral Density (RSD), which will give us the noise floor in terms of $[T/\sqrt{Hz}]$. Given that our data file is one second long and that we have 160 pulses within this second, we are limited by the Nyquist–Shannon sampling theorem to a maximum frequency in the RSD of $80[Hz]$. The length of the data file gives us a frequency spacing of $1[Hz]$.

In figure 6.6 and 6.7 we see the calculated noise floor for different amplitudes of the

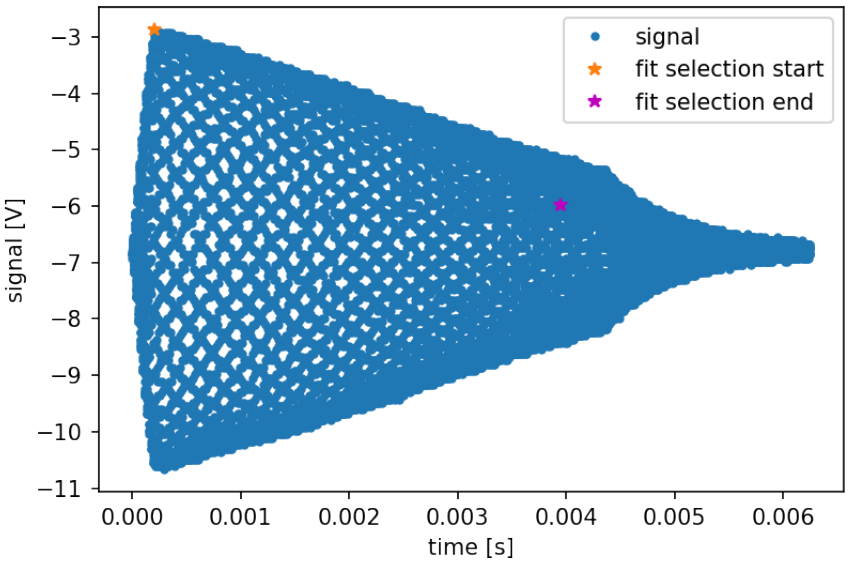

(**a**)

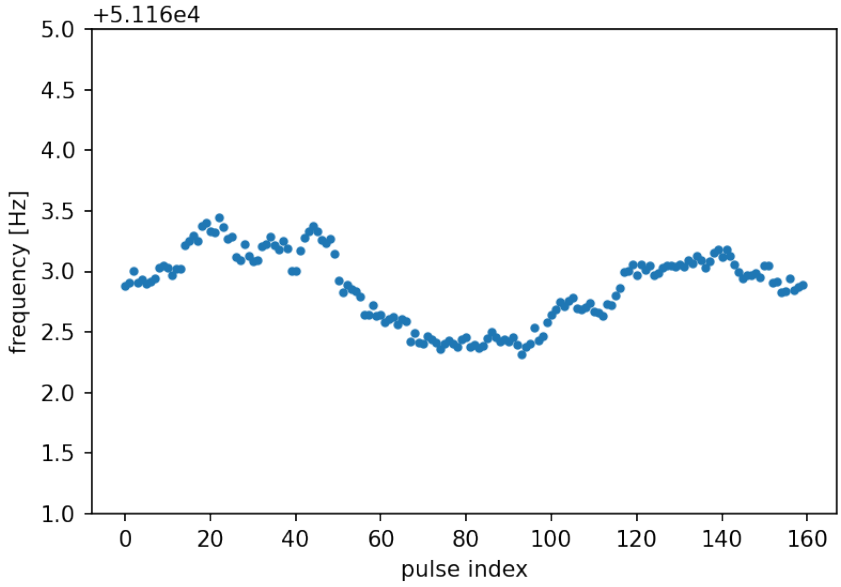

(**b**)

Figure 6.5: **(a)** Fit to the spin decay. **(b)** The 160 frequencies found by fitting to the pulses. As we can see the frequency is not stable.

driving RF excitation. There is no observable difference between the noise floors at the different drive frequencies above the uncertainty. We can also see that the noise floor for the range of 20$[Hz]$ and above is between 16$[pT]$ (green line) and 3$[pT]$ (orange line), which are the two noise floors found in [6] and are therefore our point of comparison to evaluate the performance of our magnetometer. There is a general trend towards a lower noise value in all the traces as we go to higher frequencies in the RSD.

The advantage of this method is that we do not need to accurately cancel transverse

magnetic fields to get good performance at low frequencies, which is required in the magnetometer mode described in section 6.4. The method will work as long as at least a few cycles of the Larmor precession are contained in the FID, which is determined by the desired sampling rate and the Larmor frequency. It is also assumed that the magnetic field variations are so slow that the frequency is stable over the course of a single FID phase.

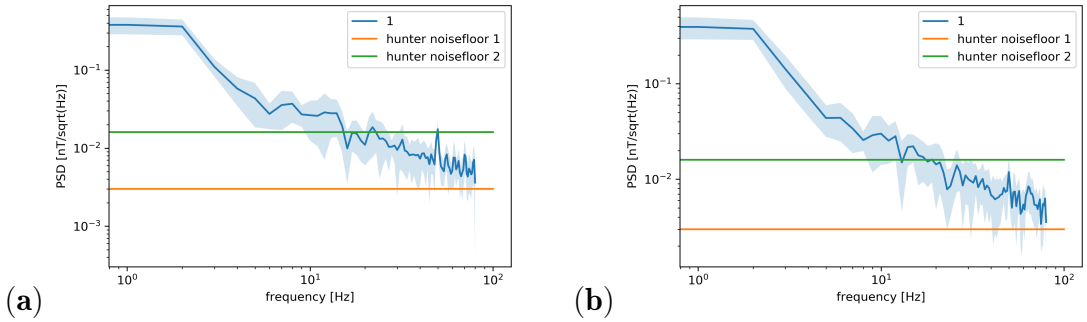

Figure 6.6: **(a)** Sensitivity as a function of frequency with 1VPP RF excitation. **(b)** Sensitivity as a function of frequency with 2VPP RF excitation.

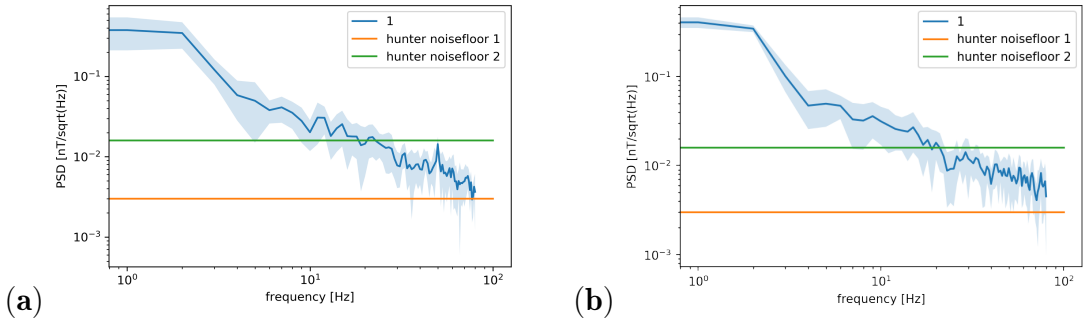

Figure 6.7: **(a)** Sensitivity as a function of frequency with 3VPP RF excitation. **(b)** Sensitivity as a function of frequency with 4VPP RF excitation.

If we were to try and improve these results, a natural first step would be to get a more stable power supply so that we have the freedom to test for both low and high Larmor frequencies. The choice of the relatively low sampling-rate, which gives the low maximum frequency of 80$[Hz]$, was made with the intention of having a better comparison of sensitivity between the different Larmor frequencies. Although we are using a different type of cell compared to [6] (they have a 1.5 mm thick micro-fabricated vapor cell with nitrogen buffer gas), it should still be a reasonable comparison as we are both aiming for the same thing which is a miniaturized magnetometer.
We will now move on to determining the magnetometer's sensitivity in the Radio frequency(RF) regime.

6.3 RF sensitivity

To fully characterise the magnetometer, we will need to know its sensitivity in the Radio Frequency domain as well as the sensitivity in the DC domain. We are interested in the magnetometer's RF performance as there are other experiments in the lab[9] that work in the RF regime. Getting these measurements out of the realm of academic interest and into the realm of real-world application would involve the construction of a sensor that could possibly have a similar layout to ours.
To measure in the RF domain we will need to increase the bias-field such that we have a Larmor-frequency at around 150$[kHz]$. The reason for this frequency is that it was the highest we could go with the power supply that was available, and given that we had limited time, and the primary purpose of the project was to get a good DC sensitivity, we did not want to spend a lot of resources and time pushing the Larmor frequency higher.
To calculate the sensitivity limit in the RF regime, we first measure the response of the system when we perturb it with an external magnetic field at a known amplitude. We know the field strength from the method discussed in section 5.3.2. The measurement with the calibrated perturbation is the blue line in figure 6.8. We also measure the atomic response with no RF-field applied. This is the green line in figure 6.8.
We can use this to calculate the minimum applied field that would be measurable when applied to the magnetometer. We do this by calculating the field strength of the applied field that would result in a signal to noise ratio(SNR) of 1.

$$SNR = \frac{PSD_{RF_{on}}(\omega = \omega_{Larmor})}{PSD_{RF_{off}}(\omega = \omega_{Larmor}),} \tag{6.4}$$

$$sensitivity = \frac{rf\_amp}{SNR(\omega = \omega_{Larmor}).} \tag{6.5}$$

From this we get that the sensitivity in the case shown in figure 6.8 is 74$[ft]$. Two reasonable questions at this point could be: How does the sensitivity depend on the probe power, and why are there no error bars in figure 6.8?
To answer the last question first, what we see in figure 6.8 is not a single shot measurement but rather the average of 100 measurements, and we know that the error on the mean scales as[2]

$$\sigma_{mean}(f) = \frac{\sigma_{STD}(f)}{\sqrt{N},} \tag{6.6}$$

where $\sigma_{mean}(f)$ is the error on the mean value at a given frequency, $\sigma_{STD}(f)$ is the standard deviation at the given frequency, and N is the number of measurements. N is not frequency dependent. Given this and the fact that when taking the data, we could not observe any difference between the trace with 100 and 110 averages, we may neglect the errors bars. Also, as the data is saved as an averaged PSD, we do not have a way to reconstruct the error bars.

This is of course only true if we assume Gaussian error. Gaussian noise is usually a good assumption when dealing with classical noise. Given that the expected

quantum noise for this experiment is in the range of $4[fT]$ [10], it is not unreasonable to say that we are still dominated by classical noise contributions.
The average is not taken of the raw traces but rather of their Fourier transformations. If we were to take the average of the raw traces instead, we would need to have a signal that is phase stable in between traces in order to detect it. By averaging after, we avoid this complication.

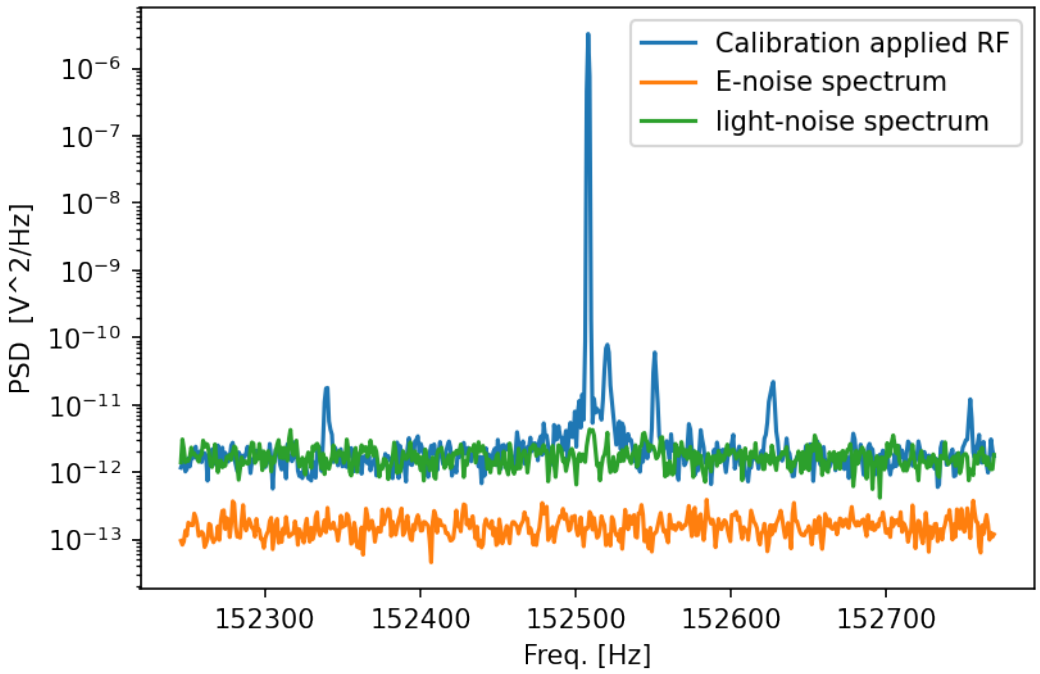

Figure 6.8: High frequency sensitivity 74 fT.

There are many factors affecting the sensitivity we could explore. Some of the options are:

- The laser power of the probe, pump or re-pump.
- The cell temperature.
- The probe detuning.
- The Larmor frequency.

The one we have decided to do a quantitative test of is the dependence of the sensitivity on the probe power. As we explained in the theory section, the probe should be far enough detuned that it will not have a major effect on the coherence of the atomic spin state, but it will have some depumping effect that will increase with the laser power.
To test the dependence of the sensitivity on the probe power we will conduct the same evaluation as before for 7 different powers. The resulting sensitivities can be

seen in figure 6.9. We see that as we increase the power we get a better sensitivity, but the best sensitivity of $74[fT/\sqrt{Hz}]$ is obtained at $300[mV]$. The sensitivity at $432[mV]$ is only slightly worse than at $82[fT/\sqrt{Hz}]$.

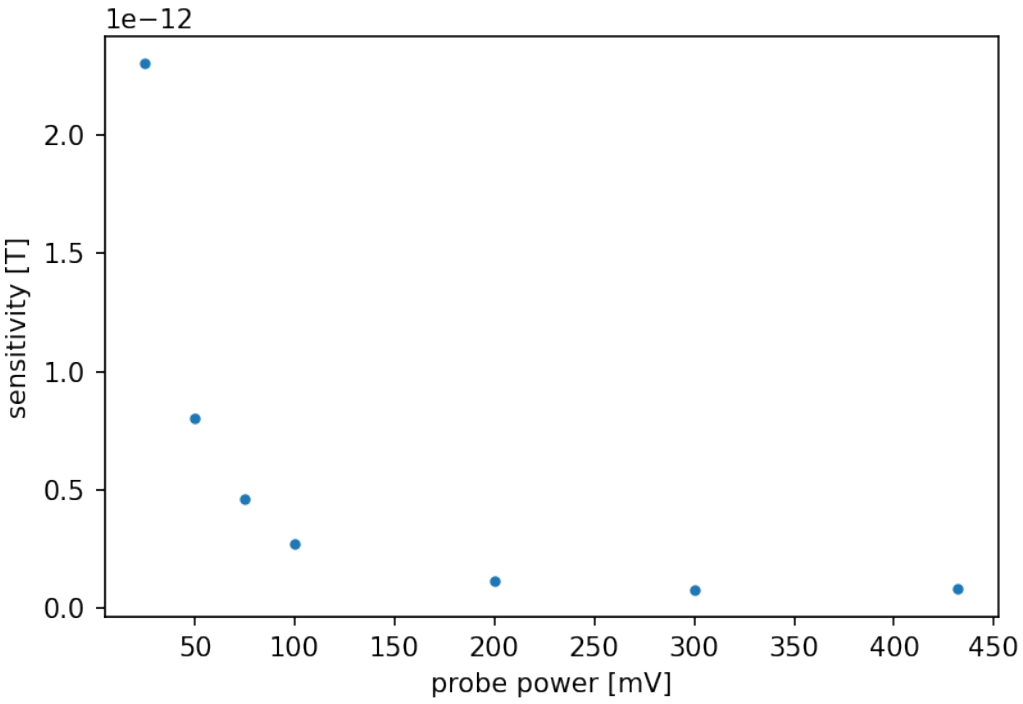

Figure 6.9: The RF sensitivity of the magnetometer as a function of the probe power.

If we were to compare this to previous results, we then see that in [1], for an applied version of a RF sensitivity measurement (eddy current imaging), the estimated sensitivity was $21[fT/\sqrt{Hz}]$. If we wanted to take a measurement that would be directly comparable to this, we would of course have to repeat their eddy current imaging method with our sensor, but it should be a reasonable benchmark. If we want to attempt to reach a comparable sensitivity, then the first step would be to increase the the Larmor frequency to the same range of $0.5 - 1.99[MHz]$ and then optimize from there. Now that we have obtained a reasonably good sensitivity in the RF regime, we will move on and evaluate the magnetometer's performance in a continuous DC measurement.

6.4 DC Sensitivity

One of the ideas that prompted this project of constructing a 3D printed magnetometer was the hope that fixing all the optical elements inside a small rigid box would help minimize the effects of mechanical vibrations on the sensitivity at low frequencies. To test this, we will recreate the measurements from [10] and compare. We have also constructed a different power-supply to avoid using the same as in the FID measurements with its one unstable output as we now need 3 stable outputs for transverse field cancellation.

6.4.1 Reconstruction of the magnetic signal

The output we get from our magnetometer when using it to measure DC or near DC signals is the result of a convolution between the kernel of the magnetometer and the input signal. It can be expressed by the following:

$$h(t) = c \cdot (f * \kappa)(t) := c \cdot \int_{-\infty}^{\infty} f(\tau)\kappa(t-\tau)\, d\tau. \tag{6.7}$$

As the convolution operation is commutative, it does not matter if we set f or κ to be kernel or input signal. We choose to use κ for the kernel and f for the input. What we want to find in the end is a general expression to retrieve $f(t)$, given $\kappa(t)$ and $h(t)$. First we need to figure out a method by which we can determine $\kappa(t)$, the kernel, also called impulse response. We do this by inputting a "delta function"(impulse) as $f(t)$. By doing this we get:

$$h(t) = c \cdot \int_{-\infty}^{\infty} \delta(\tau)\kappa(t-\tau)\, d\tau = \kappa(t). \tag{6.8}$$

Note that this kernel is only valid for the exact set of conditions it was obtained under, laserpowers, and B_x,B_y,B_z. We decided to use a square wave of height $3[V]$ and width $100[\mu s]$ to mimic a delta function in accordance with [10]. This is the reason that delta function was put in quotations earlier, as it is not possible to generate a true delta function.
So now for a given measurement we have $h(t)$, the measured signal, and $\kappa(t)$ the kernel. Now we just need an operation that is the reverse of a convolution, which is called a deconvolution. First we note that the convolution theorem states that a convolution in the Fourier-domain is just a multiplication:

$$\mathscr{F}(f * \kappa)(t) = c \cdot f(\nu) \cdot \kappa(\nu), \tag{6.9}$$

so as long as none of the frequency components of $\kappa(\nu)$ are zero, we can write $f(t)$ as:

$$\mathscr{F}^{-1}\left(\frac{\mathscr{F}(h(t))}{\mathscr{F}(\kappa(t))}\right) = c \cdot f(t). \tag{6.10}$$

To find c, the factor converting from volt on the output of the photo detector to magnetic field, we input a calibrated signal with a known frequency and amplitude in magnetic field and measure the output. We know the induced magnetic field by the method discussed in section 5.3.3. We use a 100 Hz sine-wave for this. The

result of this can be seen in fig 6.10**a**, where the red line is the input signal to the RF coil, and the blue line is the magnetometer output from the balanced photo diode. Looking at fig 6.10**b**, we see the result of deconvoluting the input with a kernel similar to the one that can be seen in fig 6.13**a**. Both the Fourier transform of the kernel and measured signal was truncated at 2000$[Hz]$ to eliminate high frequency noise. We are not concerned about losing information at higher frequencies as we are measuring the the DC or very low frequency domain. Looking at figure 6.10**b**, we see that the reconstructed signal fits well with the input, but there is a small bump after the end of the sin-wave in the reconstructed signal. We will come back to this small overshoot in the end of the deconvoluted signal in section 6.5.

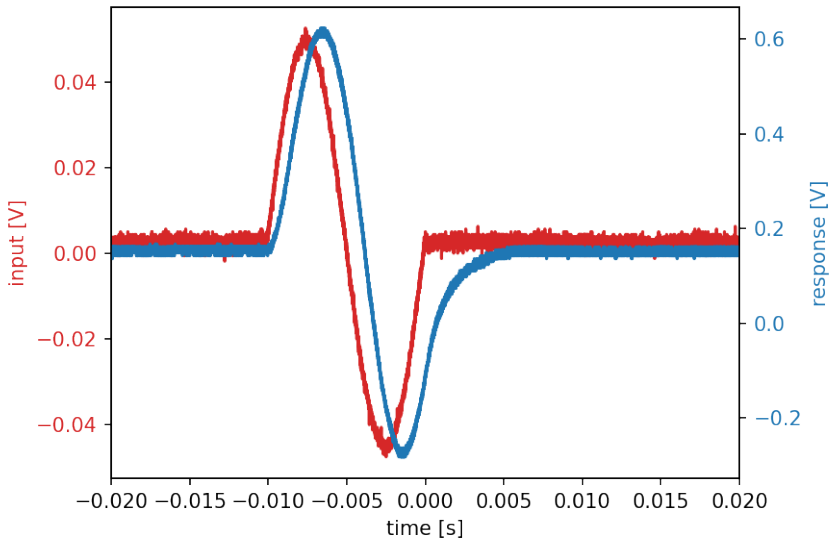

(**a**)

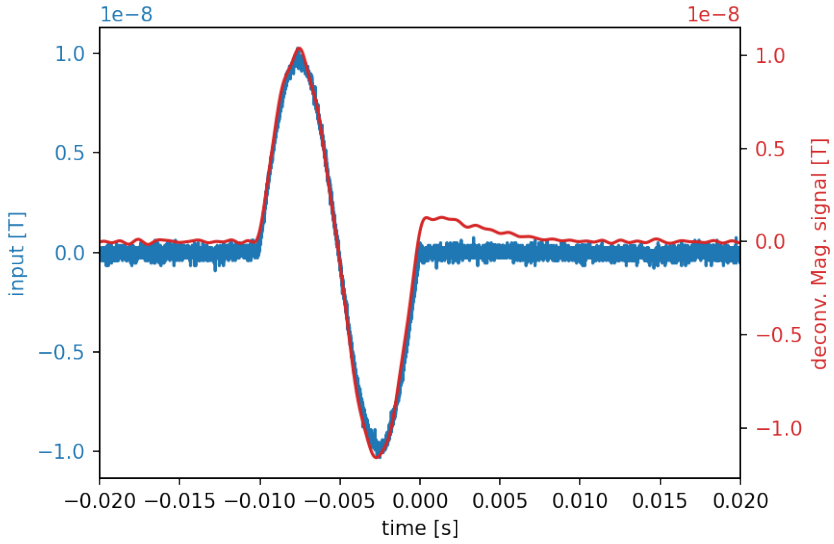

(**b**)

Figure 6.10: **(a)** Red: Input signal on the RF coil. Blue: Atomic response as measured on the balanced output. **(b)** Blue: Input signal Red: Deconvoluted signal. Note the small bump at the end of the oscillation.

The c factor is determined by the ratio between the amplitude of the input signal and the amplitude of the output signal. This ensures that the deconvoluted signal has the correct amplitude in magnetic field units. The result can be seen in figure 6.10**b**. This factor should not be frequency dependent as the frequency response of the sensor should be contained in the kernel.
We now have all the tools to reconstruct an arbitrary input signal: The kernel, The normalization factor, and the mathematical operation for the deconvolution. We can now find the noise floor of the sensor by measuring a trace of the noise, deconvoluting it and thereafter calculating the RSD. This is again assuming that we can't measure any signal with a SNR under 1. We do the same with a trace of the electrical noise from the balanced detector. This is to check how much of our total noise is due to the photo-detector. The noise trace is taken with the RF coils disconnected and terminated but all the lasers on. The e-noise trace is taken by blocking the probe laser, but not blocking the pump/re-pump laser, but still saving the output of the balanced detector.
The normal noise floor and e-noise floor can be seen in figure 6.11. The shaded area around the trace indicates 1 standard deviation, at a given frequency, as calculated from the RSD of 10 individual traces. The line is the mean of the 10 traces. We indicate the STD on the mean because if we were to use the magnetometer to measure an unknown low frequency signal, e.g a magneto cardiogram of a beating heart[10], we would have to use the magnetometer in single shot operation.
We see that in general, the noise floor seem to be slightly above $100[fT]$ in the range

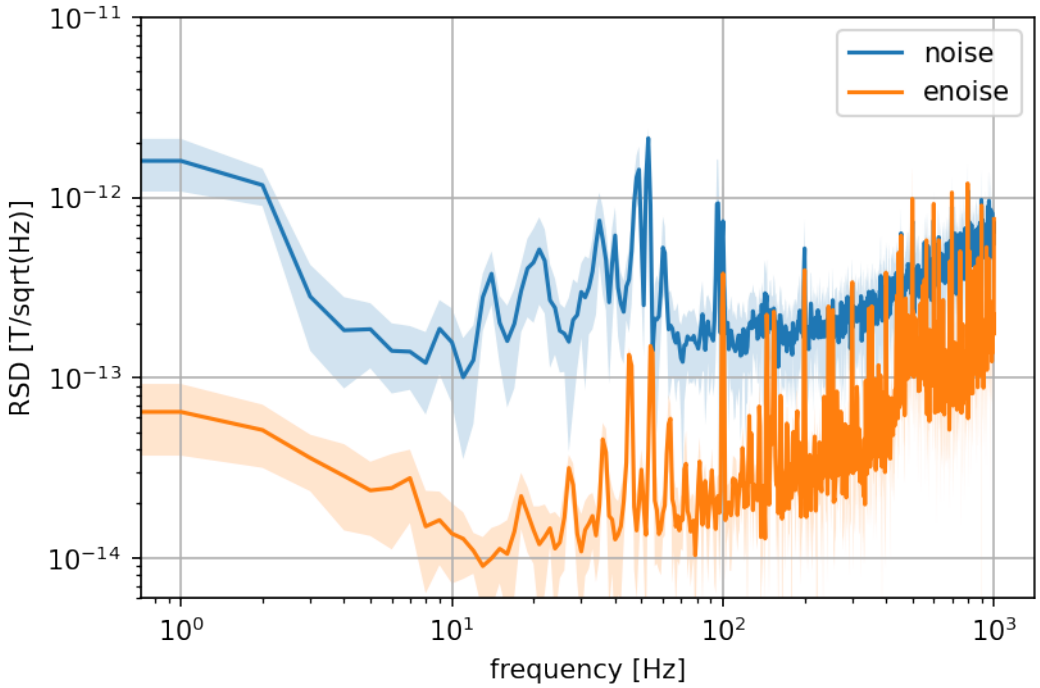

Figure 6.11: Comparison of the electrical noise RSD (Root spectral density) and the measured noise RSD.

between $10[Hz]$ and $100[Hz]$, but there are lots of noise peaks that are suspected to not be inherent to the magnetometer, and they should therefore be able to be eliminated. We also see that the e-noise is in general only one order of magnitude or less below the noise floor, so if the noise floor is improved, then changing the detector to a better one might make sense so that our total noise is not dominated by the e-noise.

What we can also see in both the e-noise trace and the normal noise is that we have peaks at $50[Hz]$, $100[Hz]$,$150[Hz]$... and so on. Given the amount of electrical equipment in the lab it is no surprise that we have some noise at 50 [Hz] and multiples thereof, but that they are also so prominent in the e-noise trace could be problematic. However, the range we are most interested in is the $10[Hz]$ to $100[Hz]$, so the noisepeaks at $100[Hz]$ and above may be a challenge for the future.

6.5 Kernel

As promised in section 6.4.1, we will now return to the problem of the small bump in the reconstructed 100$[Hz]$ signal. As explained in section 6.4.1, the normalization constant c should not be dependent on frequency, so if we input a different frequency sine-wave than 100$[Hz]$, we should still have the same ratio between the amplitude of the input and deconvoluted signal. If we have calculated c correctly, it should be 1. As a difference in amplitude between 100 [Hz] and 10 [Hz] could be observed on the scope prior to deconvolution, it seemed like a reasonable thing to test, as the kernel might take care of this apparent frequency dependence of the normalization constant. Looking at the ratio between the reconstructed amplitude and the input amplitude in figure 6.14, we see that the 100$[\mu s]$ kernel we have been using so far shows a very significant frequency dependence of the normalization constant.

The normalisation constant is calculated as shown in figure 6.12. In the upper

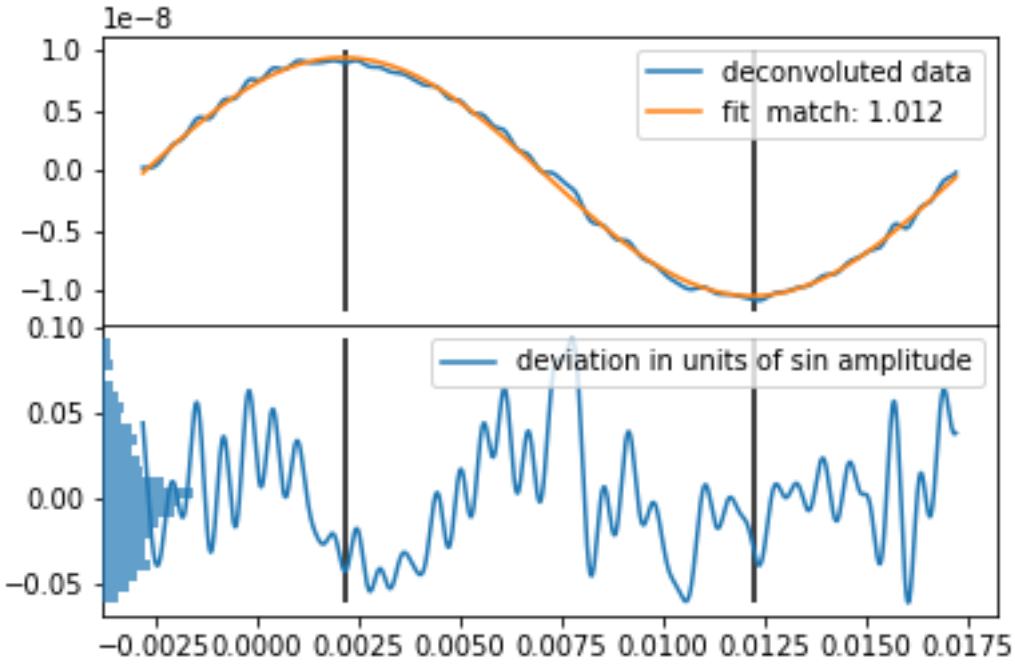

Figure 6.12: Fit to the deconvoluted signal and calculation of the deviation.

part of the plot we see our fit of a sine wave to the deconvoluted signal. To ensure that the fit is acceptable, we look at the residual from the fit which is plotted in the lower part of 6.12. If the deviation came from there being secondary oscillations that match with the primary such that maximum was overestimated and the minimum was underestimated, we would spot it in the residual, given that we only fit with a single sine-wave. The residual is normalised with the amplitude of the fitted sine wave. What we see on the y-axis of the lower plot is a histogram of the residual to check what kind of statistical distribution our deviation from the sine comes from. It seems mostly Gaussian, though with a small secondary peak. The two vertical bars

indicate the found minimum and maximum. The factor shown in 6.14 is calculated by taking the range of the inputted sine wave and dividing it by the range of the deconvoluted sine wave.

The suspected reason for the deviation in the c factor is that the the impulse used, width $100[\mu s]$ and height $3[V]$, is not a good enough approximation of a delta-function to give us the the true kernel of the system. To test this, we decided to try and input impulses of a few different widths ($\{40, 100, 200, 400\}[\mu s]$) and collect a series of different frequencies of sine-waves to deconvolute with these kernels. The kernels of impulse width of $200[\mu s]$ and above simply distorts the sine-wave so much that it does not make sense to talk about the ratio of the amplitudes anymore.
In figure 6.13 we see the difference between a kernel from a $100[\mu s]$ width impulse and a $40[\mu s]$ width impulse. Just by visual inspection, the one obtained from the $40[\mu s]$ width impulse seems close to being an exponential decay. Looking at deconvoluted sines in figure 6.14, we see that using the $40[\mu s]$ width impulse kernel makes the overshoot go away, and in figure 6.15 we see that the deviation in ratio between the deconvoluted amplitude and the input amplitude has been reduced by almost $\frac{2}{3}$.

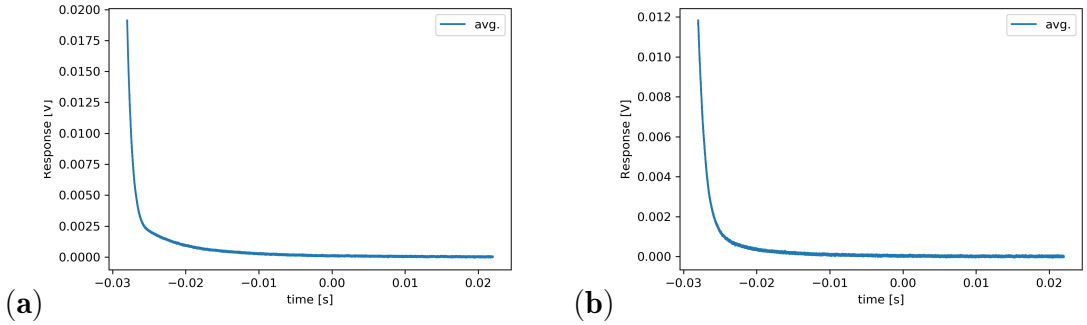

(a) (b)

Figure 6.13: **(a)** 100 microseconds kernel. **(b)** 40 microseconds kernel

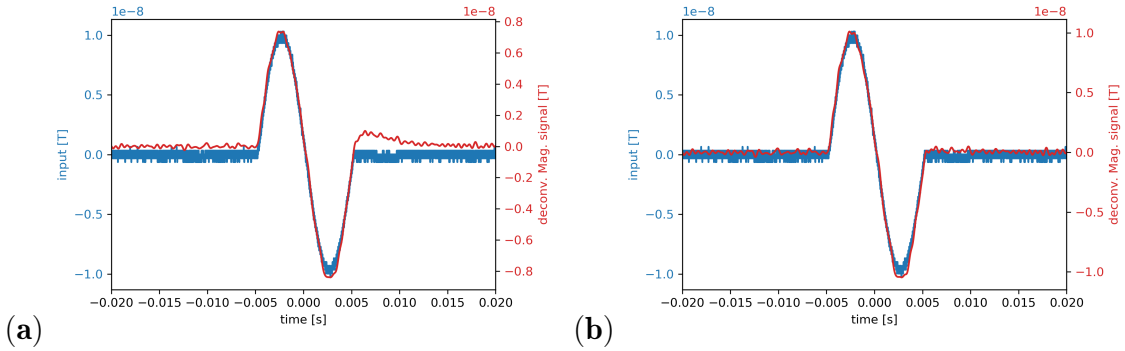

(a) (b)

Figure 6.14: **(a)** 100 Hz deconvoluted with the 100 microseconds kernel. **(b)** 100 Hz deconvoluted with the 40 microseconds kernel. Note that the bump is now gone.

We clearly see that we should change from using a $100[\mu s]$ wide impulse to a $40[\mu s]$ wide one as it not only gives a behavior of the normalisation constant much closer to what we would expect from the theory, but it also makes the deconvoluted signal fit better with the known input. The reason for not going lower in width is

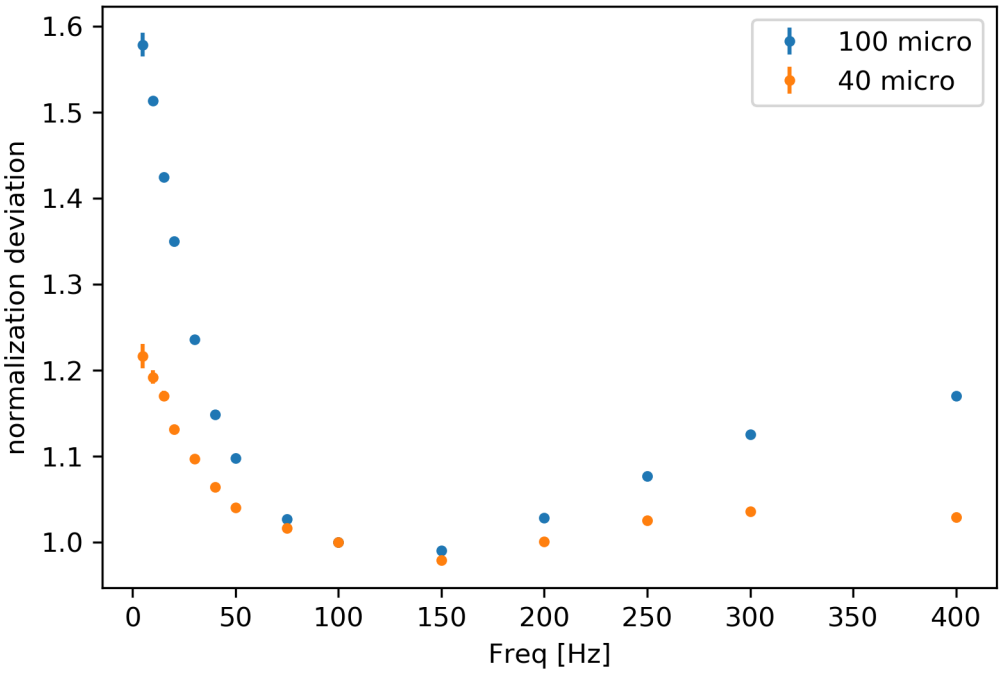

Figure 6.15: Normalisation factor as a function of frequency.

that the function generator we use does not allow for this, and we don't have one that is better, in this respect, readily available.

6.6 Long-term stability measurement

In the same way we tested the sensitivity's dependence on power in section 6.3, we would have liked to find the optimal setting for the probe power in for the DC sensitivity. The probe power used so far is approximately the same as in the RF-case. The trace in 6.16 is a raw trace of the balanced detector output over the course of approximately 8 minuets. This is taken at around 3 times the probe power used previously. It is clear to see that there is a lot of variance in the value. Given that the probe is power stabilised and that the balanced output crosses zero several times, we can exclude this being a problem arising from the probe only. Given the large range of values, it is not possible to extract any usable noise-trace, as it will have digitization error arising from the necessary scope-settings to capture the entire range of values. This should also not be the result of fiber oscillations, as the fibers were left undisturbed for several minutes to let any mechanical vibrations decay. As the measurement was taken at around 3 am, it is not the result of others people's activities in the lab. The measurement was also taken with the lights off to ensure that no stray external light could effect the measurement.

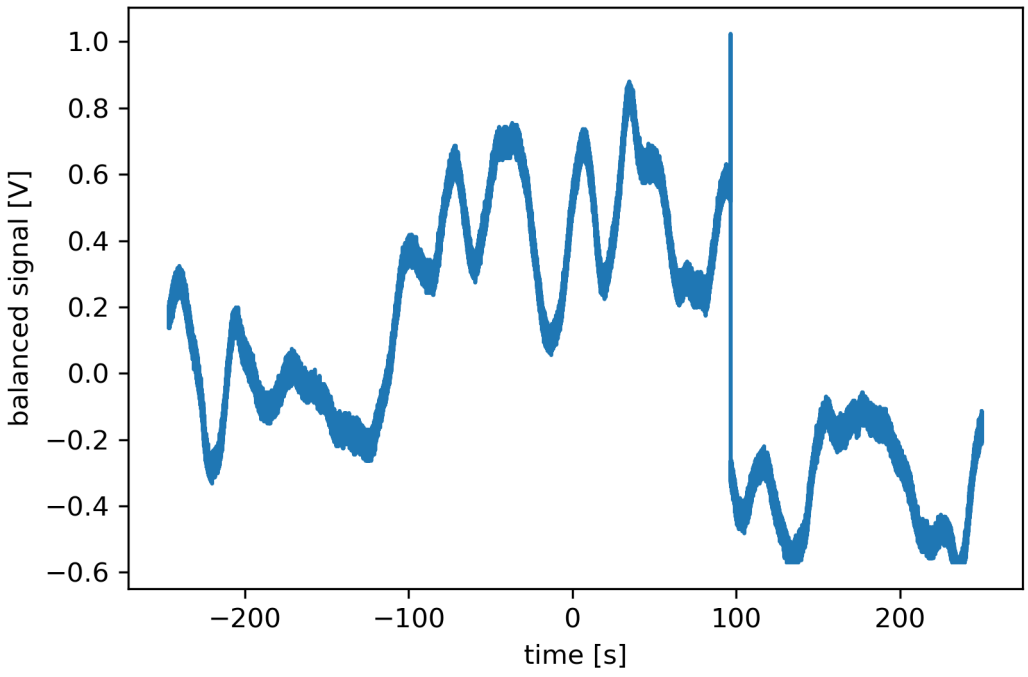

Figure 6.16: Long trace of the balanced output at a very high probe power.

6.7 Noise analysis

The noise floor of the magnetometer will have several contribution. Some of these, such as spin projection noise, are the result of quantum mechanical effect and are as such inherent in the system as we have chosen to explore it. Given that the quantum spin-projection noise for our caesium ensemble is estimated to be $4[fT][10]$, there should still be room for improvement through elimination of classical noise sources. Inspired by [12], we choose to do an analysis of the expected impact the amplitude noise of the pump laser has before we decide to invest the time and resources to perform power stabilisation of the pump laser.

6.7.1 Pump amplitude noise

To reduce the noise we see in the spectrum, we will look at how large of an impact the amplitude noise of the pump has on the overall noise. The reason to do this is twofold: Firstly we have observed by looking at the output power of the pump in the pump/re-pump monitor that the power will fluctuate somewhat over time. The second reason is that the setting of the pump in general seems to have a large impact on the performance of the magnetometer.

To figure out the impact that pump amplitude noise has on the overall noise, we induce amplitude noise at one specific frequency - in our case it was at 90 Hz. We induce the amplitude noise by varying the voltage on an acousto-optic modulator (AOM), thereby changing the amount of light that is scattered into the different modes of the AOM.
This peak is then detected in the PSD of the pump monitor, let's call it $PSD_{pump}^{modulated}$.

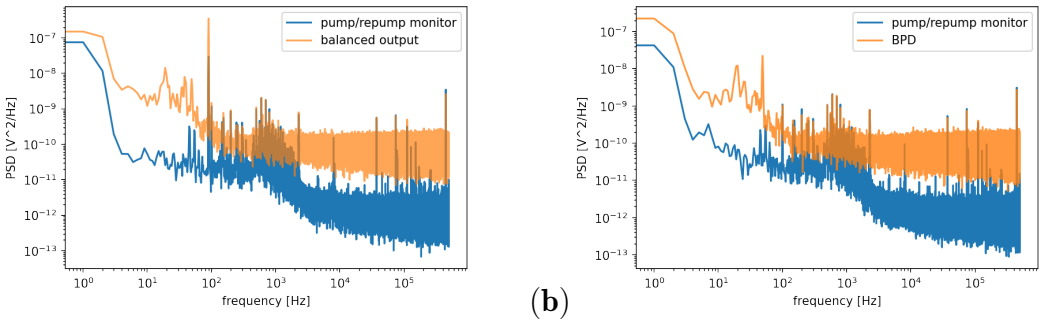

(**a**) (**b**)

Figure 6.17: **(a)** Pump monitor and balanced output with the pump modulation at 90 Hz. **(b)** Pump monitor and balanced output without the pump modulation at 90 Hz.

We can not assume that the entire noise at the specific frequency is the induced noise, only the noise above normal level. We therefore also collect a noise spectrum of the pump without the induced noise. We call this PSD_{pump}^{normal} .
If we take the difference between these two PSD's at the modulation frequency, we will know how much of it is due to the modulation.

Now that we have determined the modulation in the pump laser, we need to find the the impact this has on the balanced output. To do this, we follow the exact

same procedure: Measure the PSD of the magnetometer while not inducing any pump amplitude modulation, $PSD^{normal}_{balanced}$,
and measure the PSD of the balanced output with the pump modulation, $PSD^{modulated}_{balanced}$.
With all this we will now construct the function

$$scale\_factor(f) = \frac{PSD^{modulated}_{balanced} - PSD^{normal}_{balanced}}{PSD^{modulated}_{pump} - PSD^{normal}_{pump}}. \tag{6.11}$$

If we evaluate this function at the modulation frequency of 90 Hz, we will get a factor which we can use to translate between power in the pump spectrum and power in the balanced output spectrum. If we also assume that we have a flat frequency response of the balanced output to pump amplitude modulations, then this factor will be the general conversion factor and not just for the 90 Hz. We find a scaling factor of 13.4.

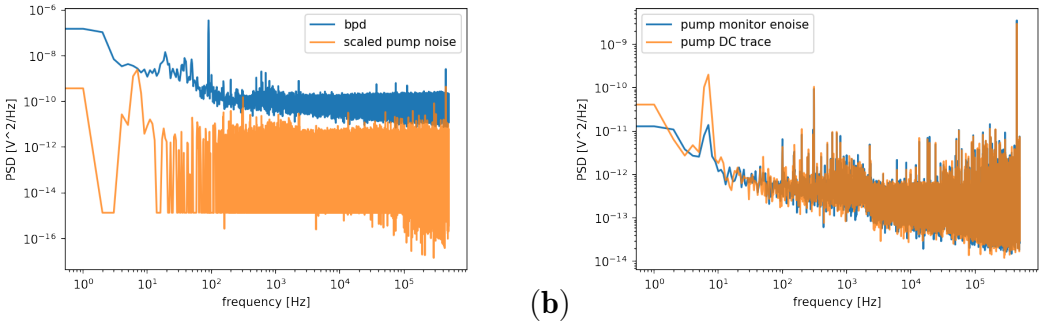

(**a**) (**b**)

Figure 6.18: **(a)** Balanced output and scaled pump noise. **(b)** Pump monitor PSD and detector e-noise PSD.

Looking at figure 6.18**b**, we see that the noise on the pump is, for the most part, not above the electrical noise of the detector. If we continue anyway with this method, we see in figure 6.18**a** that the scaled noise is, for the most part, one to two orders of magnitude below the total noise on the balanced output.
If we were to draw a conclusion on this, it would be that noise on the pump will have some impact on the total noise floor as can clearly be seen from the induced peak in 6.17**a**, but the impact of the observed pump noise on the total noise floor will be negligible at the current level. This is in good accordance with [14], where they did not quantify the impact of amplitude noise from the pump on the total noise level, but they power-stabilized the pump and saw no quantifiable drop in noise.

6.8 After noise elimination

Some potential noise sources were eliminated or suppressed without doing a thorough analysis of the expected impact as in section6.7.1. Some of these changes made to reduce the noise are:

- Two end caps were added to the shield.
- The probe laser was power stabilised.

- Some noise sources were turned off in the lab. This was primarily power supplys to other equipment.
- The new measurement was performed late at night to reduce the impact of human activity in the lab.
- Polarizer before pump/re-pump fiber to reduce polarization noise.

Given the length of the shield of around 1 [m], we didn't think that the end caps should be strictly necessary, but since we had an unused set of end caps in the lab, we decided to add them. When we switched our measurement time to late in the evening or night, we got the chance to turn off some equipment in the lab without interfering with other experiments. We also observed that the pressure change from opening the door to the lab would induce mechanical oscillations in the fibers. By measuring late at night, no-one would be opening the door during measurements. Looking at figure 6.19, we see that although our changes do not seem to have reduced the noise floor below around 120 [fT], most of the peaks in the range between 3 [Hz] and 100[Hz] are now gone, apart from the noise-peak at 9 [Hz]. The source of the 9 [Hz] and 3 [Hz] noise are not know, but it is suspected to be a piece of equipment used by several other experiments (a cryostat). This can not be turned off without causing serious disruption to the other experiments.

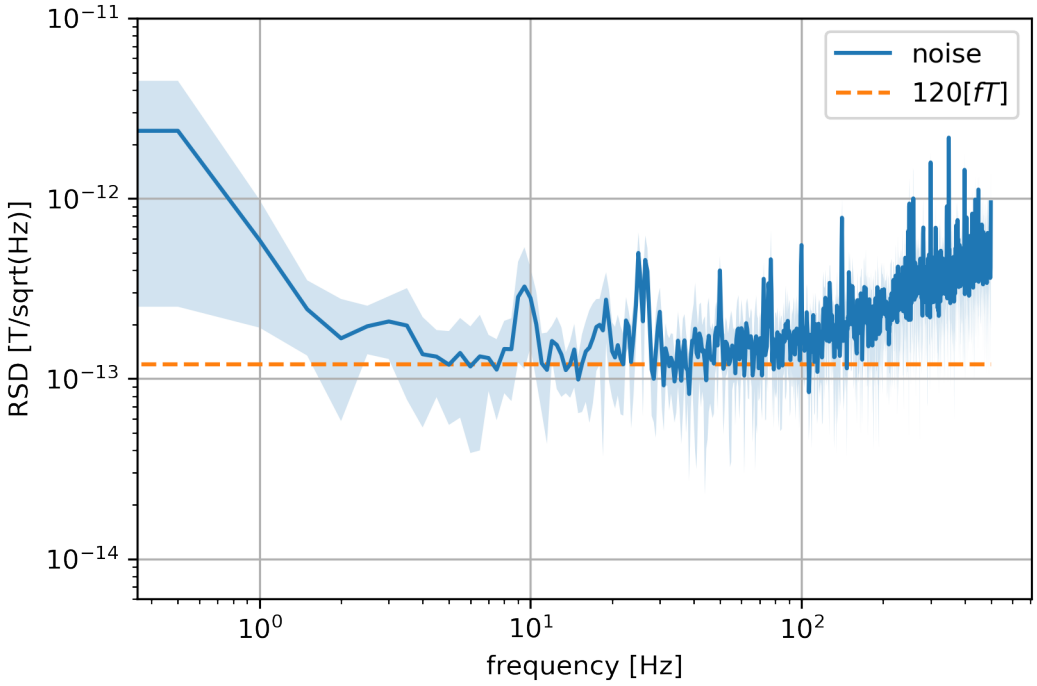

Figure 6.19: Lower noise floor after optimization.

6.9 Canceling transverse fields

Given that we are working from the assumption that a residual magnetic field of zero would give us the best sensitivity, we decided to test the impact of a poorly canceled magnetic field. The way we decided to check this was to calculate what the sensitivity of the magnetometer would be if there was no input on the cancellation coils. This will of-course result in a non-zero Larmor frequency given by the residual magnetic field of the shield.

6.9.1 No transverse field cancellation

Apart from the fact that we do not need to find the optimal settings for the transverse field cancellations which is controlled by three DAC's (Digital to analog converters), given that they are disconnected, the process will be identical to the one we usually have. First we need to collect a kernel for the given settings. Looking at figure 6.20**(a)**, we see the kernel when we apply no cancellation field. As expected it is no longer an exponential decay.
To determine the Larmor frequency of the system, we can look the the Fourier transform of the kernel. Looking at figure 6.20**(b)**, we can read off a Larmor frequency of approximately $\approx 140[Hz]$, so we do well and truly have bad DAC values in this case of no input.

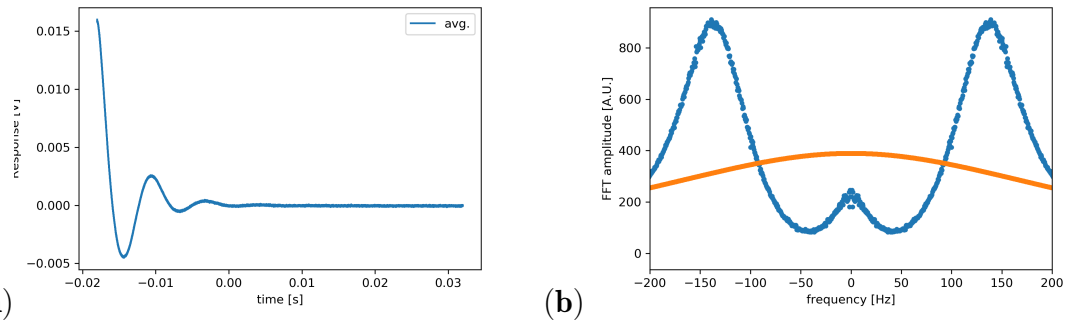

(**a**) (**b**)

Figure 6.20: **(a)** Bad DAC kernel. **(b)** FFT of bad DAC kernel(blue) and an attempted Lorentzian fit (orange).

Even though the DAC value, and thereby the Larmor frequency, is not near the optimum, we still input the $100[Hz]$ sine wave and see if we can reconstruct the input from the measured sensor output. Looking at 6.21**(a)**, we see that the output of the magnetometer still gives a large output (in volt) and that during the "drive" of the input signal, the magnetometer response follows the signal quite well. After the drive ends there are some secondary oscillations that we do not see in the "well canceled" signal.
Looking at figure 6.21**(b)**, we see that the deconvoluted signal is reasonably well reconstructed apart from a slight overshoot. It may seem like there is also an overcorrection after the overshoot, but this is mostly due to the fact that the zero-point for the left and right y-axes doesn't line up perfectly. If we now compare

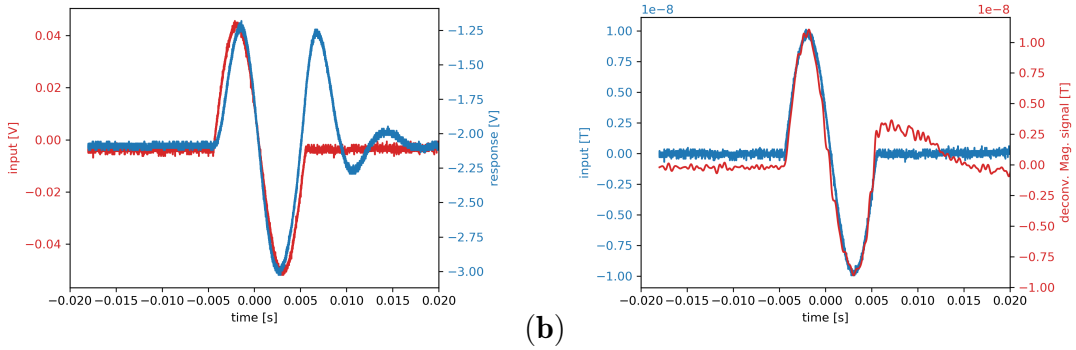

(**a**) (**b**)

Figure 6.21: **(a)** 100 Hz signal at bad DAC values. **(b)** Deconvoluted 100 Hz at bad DAC values.

the measurement in figure 6.20 to the expected signal, we see that it is in good agreement with the theoretical prediction of what the kernel should be for arbitrary fields in the y-direction.

$$\kappa(t) = aS_x\gamma J_x cos(\Omega_L \tau)e^{-(R+\Gamma_2)\tau} \tag{6.12}$$

If we take a noise trace without canceling the transverse field and calculate the noise floor, we get the result shown in figure 6.22. We see that we have worse sensitivity in the low frequencies, but this is to be expected when we look at the frequency response in figure 6.20**b**. What was reported in [1] was that they saw more noise at multiples of $50[Hz]$ when they did not do proper transverse field cancellation. This is not something that we observe.

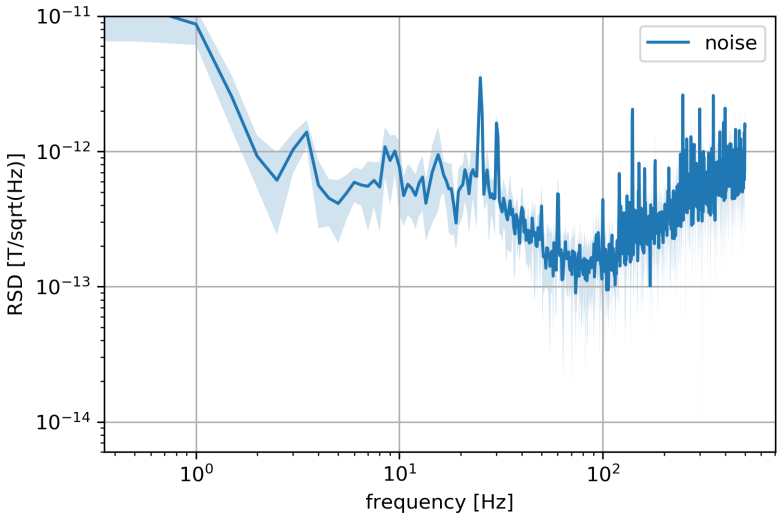

Figure 6.22: Noisefloor with poor cancellation of transverse fields

7 Conclusion

In this project we have achieved the goal of making a fiber-coupled vapor-cell magnetometer. We have seen that the magnetometer preforms well in several different modes of operation. In the pulsed DC mode we got a sensitivity below $16[pT/\sqrt{Hz}]$ above $12[Hz]$. This is approximately on par with the sensitivity achieved in [6]. In the RF mode we achieved a sensitivity of $74[fT/\sqrt{Hz}]$ at a Larmor frequency of $\approx 150[kHz]$. From [10] we get that the expected quantum spin-projection noise limit is $4[fT/\sqrt{Hz}]$, meaning that we have reached a sensitivity where we can ascribe around 5 percent of the total observed noise to be quantum noise. Finally we have also achieved a noise floor of around $120[Ft\sqrt{Hz}]$ in the frequency range of $5[Hz] - 100[Hz]$ for the continuous operation mode with well canceled transverse fields. This is approximately 30 times higher than the quantum projection noise limit. It is also approximately a factor 2 better than the sensitivity of $250[ft/\sqrt{Hz}]$ reported in [1]. In [10] they also report a noise floor of $120[fT/\sqrt{Hz}]$, but in the frequency range of $100 - 500[Hz]$. From this we can conclude that we have achieved a better sensitivity in the low frequency range than the previous experiments from our lab. As this was one of the goals of the project, we may consider this a success.

As further work we would suggest that the magnetometer could be used in a gradiometer type setup[15] where it is placed close to another caesium vapor cell with a well pumped atomic ensemble. If the two cells are placed very closely together, we can assume that the ambient fields on both are equal. This allows for the rejection of common-mode noise from the surrounding environment and could therefore potentially push the sensitivity even lower. Another logical next step would be to apply the sensor to measure a quantity of interest and thereby show that the sensor works in a practical application.

References

[1] J. Arnbak. Magnetocardiography and eddy-current imaging using an optical cesium vapor magnetometer. Master's Thesis, March 2018. Quantum Optics Group Quantop, Niels Bohr Institute NBI.

[2] R. Barlow. *STATISTICS, a guide to the use of statistical methods in the physical sciences*. The manchester physics series.

[3] D. Drung, C. Abmann, J. Beyer, A. Kirste, M. Peters, F. Ruede, and T. Schurig. Highly sensitive and easy-to-use squid sensors. *IEEE Transactions on Applied Superconductivity*, 17(2):699–704, 2007.

[4] C. J. FOOT. *Atomic Physics*. OXFORD MASTER SERIES IN PHYSICS.

[5] D. J. Griffiths. *Electromagnetism for physicists*.

[6] D. Hunter, S. Piccolomo, J. D. Pritchard, N. L. Brockie, T. E. Dyer, and E. Riis. Free-induction-decay magnetometer based on a microfabricated cs vapor cell. *Phys. Rev. Applied*, 10:014002, Jul 2018.

[7] S. J. Ingleby, I. C. Chalmers, T. E. Dyer, P. F. Griffin, and E. Riis. Resonant very low- and ultra low frequency digital signal reception using a portable atomic magnetometer, 2020.

[8] K. Jensen, R. Budvytyte, R. A. Thomas, T. Wang, A. M. Fuchs, M. V. Balabas, G. Vasilakis, L. D. Mosgaard, H. C. Stærkind, J. H. Müller, and et al. Non-invasive detection of animal nerve impulses with an atomic magnetometer operating near quantum limited sensitivity. *Scientific Reports*, 6(1), Jul 2016.

[9] K. Jensen, M. Zugenmaier, J. Arnbak, H. Stærkind, M. V. Balabas, and E. S. Polzik. Detection of low-conductivity objects using eddy current measurements with an optical magnetometer. *Phys. Rev. Research*, 1:033087, Nov 2019.

[10] S. M. S. H. e. a. Jensen, K. Magnetocardiography on an isolated animal heart with a room-temperature optically pumped magnetometer. *Sci Rep*, 8:16218, Nov 2018.

[11] B. Julsgaard. Entanglement and quantum interactions with macroscopic gas samples. PhD thesis, October 2003. Quantum Optics Group Quantop, Department of Physics and Astronomy University of Aarhus, Denmark.

[12] S. P. Krzyzewski, A. R. Perry, V. Gerginov, and S. Knappe. Characterization of noise sources in a microfabricated single-beam zero-field optically-pumped magnetometer. *Journal of Applied Physics*, 126(4):044504, 2019.

[13] J. S. . J. Napolitano. *Morden quantum mechanics*.

[14] H. C. Stærkind. Optical magnetometry for biomedical applications. Master Thesis, november 2016. Quantum Optics Group Quantop, Niels Bohr Institute NBI.

[15] T. Takiya and T. Uchiyama. Common-mode magnetic field rejection-type magneto-impedance gradiometer. *Journal of International Council on Electrical Engineering*, 7:1–6, 01 2017.

[16] R. A. Thomas. Optical spin-mechanics quantum interface: entanglement and back-action evasion. PhD Thesis, August 2020. Quantum Optics Group Quantop, Niels Bohr Institute NBI.

[17] W. Wasilewski, K. Jensen, H. Krauter, J. J. Renema, M. V. Balabas, and E. S. Polzik. Quantum noise limited and entanglement-assisted magnetometry. *Phys. Rev. Lett.*, 104:133601, Mar 2010.

A Alignment tool pictures and drawing

(**a**) 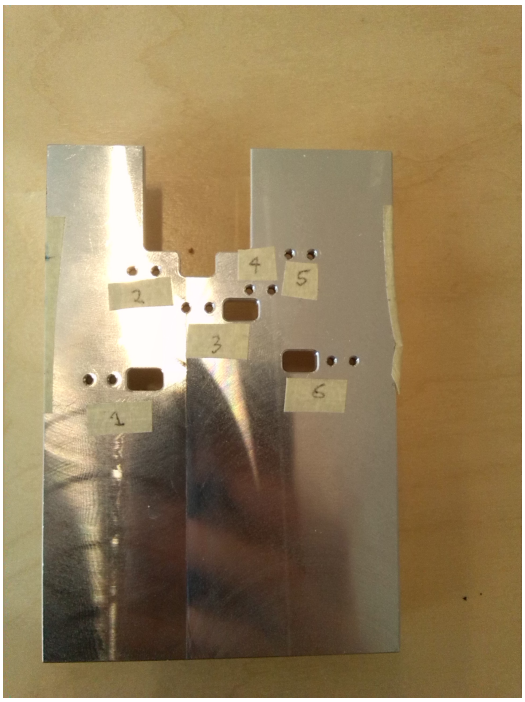 (**b**) 

Figure A.1: **(a)** Outside view of the lower part of the alignment tool **(b)** Inside view of the lower part of the alignment tool

(**a**)  (**b**) 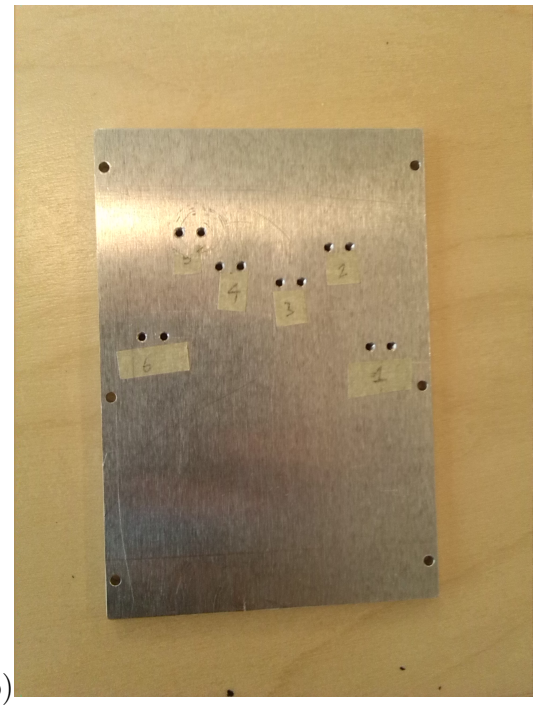

Figure A.2: **(a)** Side view of the lower part of the alignment tool **(b)** Outside view of the top part of the alignment tool

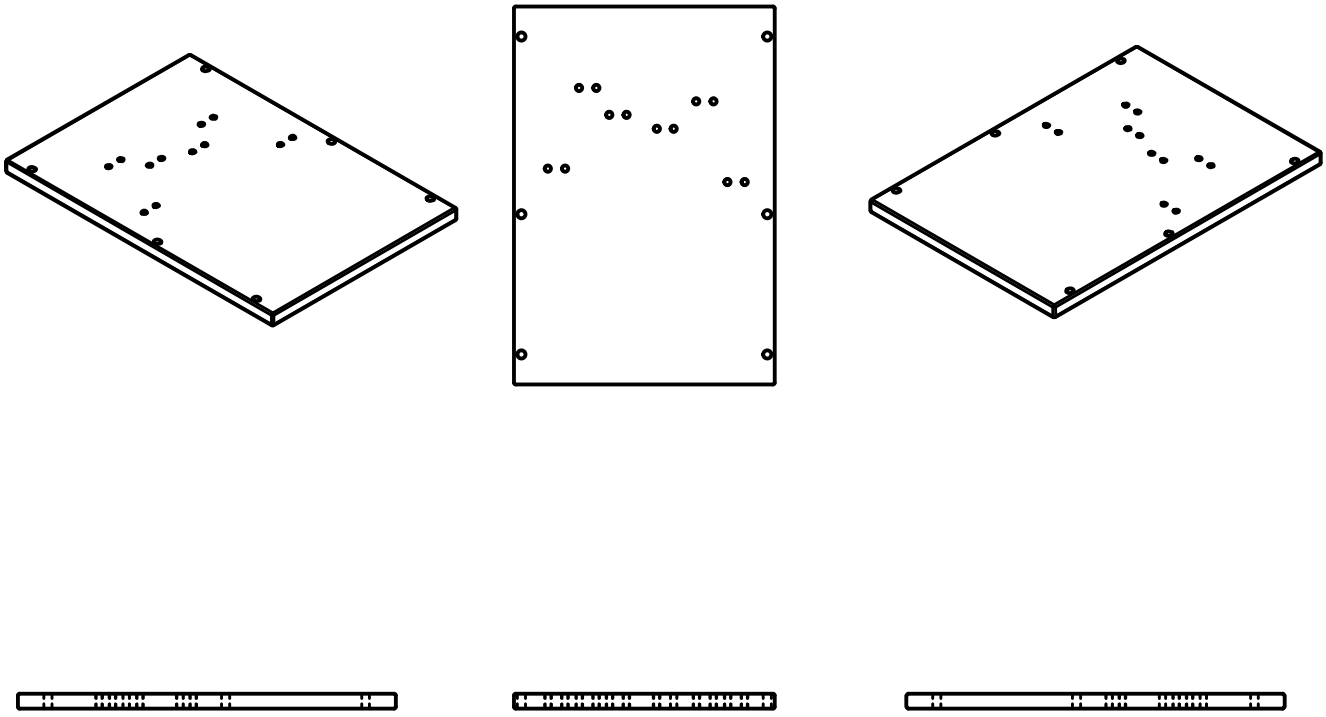

DRAWN jeppe	29-06-2021				
CHECKED					
QA		TITLE			
MFG					
APPROVED					
		SIZE A4		DWG NO	REV
		SCALE 1 / 2		SHEET 2 OF 2	

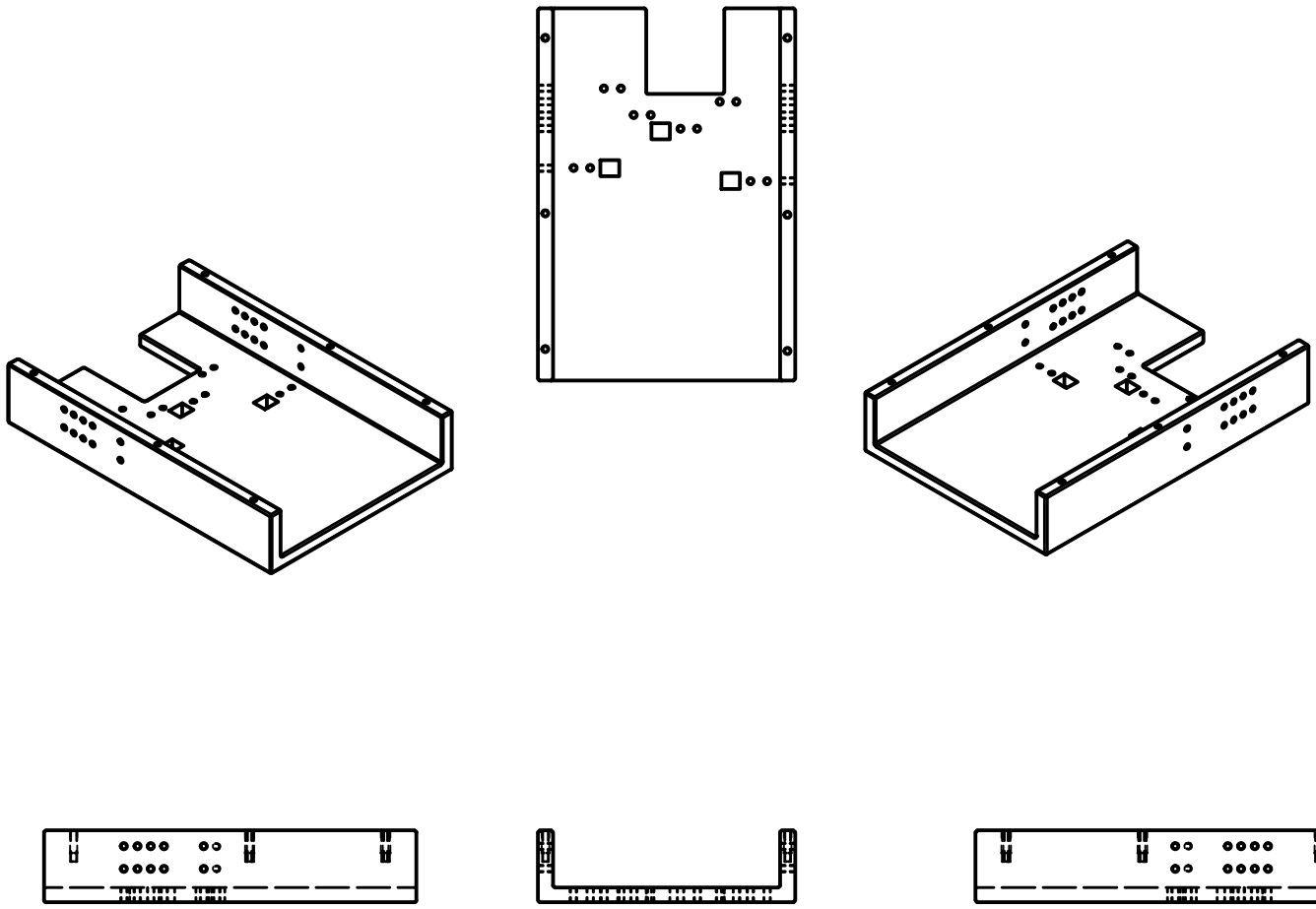

DRAWN jeppe	29-06-2021				
CHECKED					
QA		TITLE			
MFG					
APPROVED					
		SIZE A4		DWG NO	REV
		SCALE 1 / 2		SHEET 1 OF 1	

B Magnetometer pictures

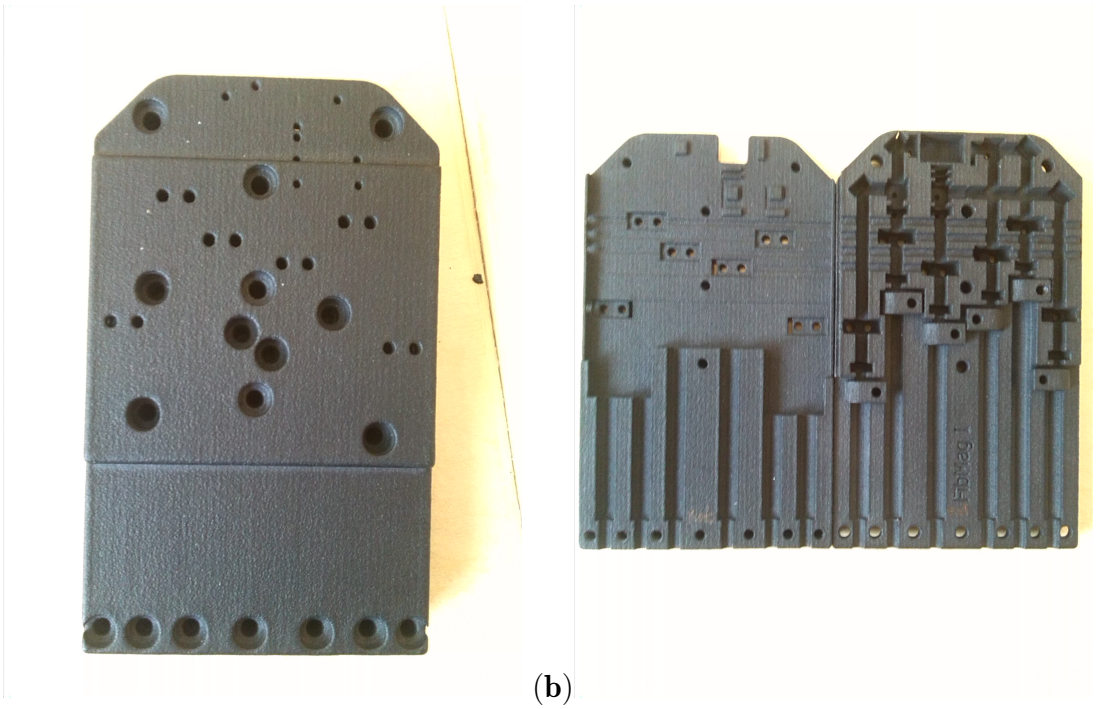

(**a**) (**b**)

Figure B.1: **(a)** Outside view of bottom of the magnetometer**(b)** Inside view of both parts of the magnetometer

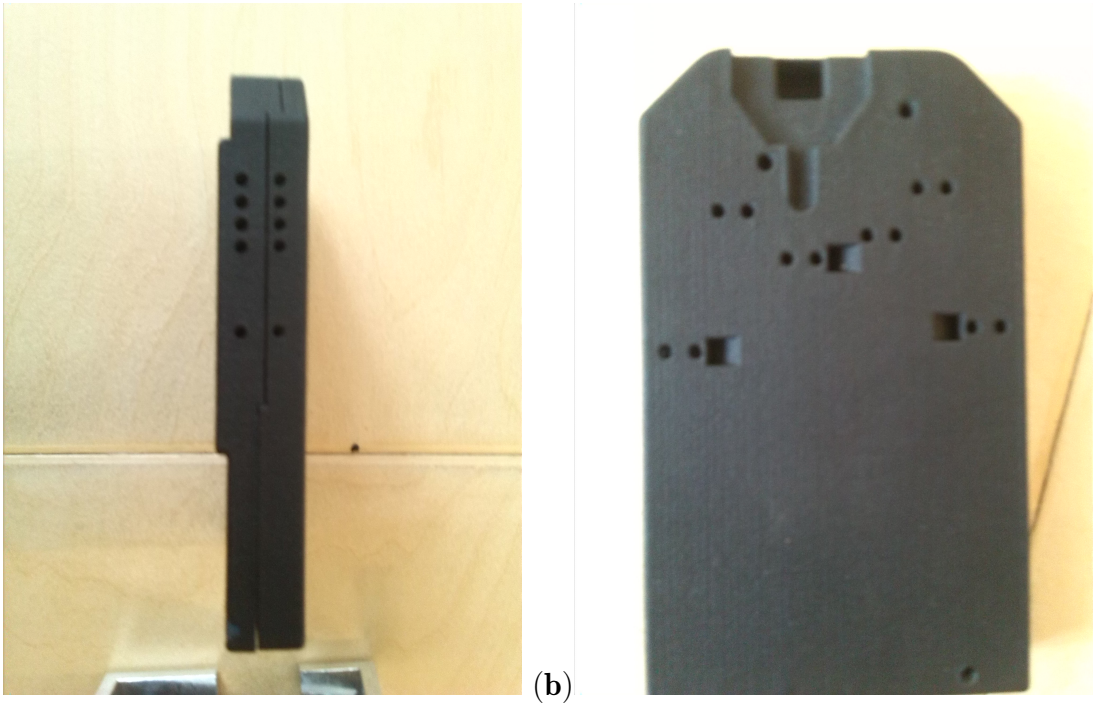

(**a**) (**b**)

Figure B.2: **(a)** Side view of the magnetometer when assembled **(b)** Outside view of the top of the magnetometer